HAW HAMBURG

Masterthesis

Kathrin Weihe

Amplitude Control of a State Signal Shaping Model Predictive Controller for Power Quality Compensation in Distribution Grids

Fakultät Technik und Informatik
Department Informations- und Elektrotechnik

Faculty of Engineering and Computer Science
Department of Information and Electrical Engineering

Amplitude Control of a State Signal Shaping Model Predictive Controller for Power Quality Compensation in Distribution Grids

Master of Science Thesis

Kathrin Weihe

September 19, 2018

Masterthesis eingereicht im Rahmen der Masterprüfung
im Masterstudiengang Automatisierung
am Department Informations- und Elektrotechnik
der Fakultät Technik und Informatik
der Hochschule für Angewandte Wissenschaften Hamburg

Betreuender Prüfer: Prof. Dr.-Ing Florian Wenck
Zeitgutachter: Prof. Dr.-Ing Gerwald Lichtenberg

Abgegeben am 19. September 2018

Statement of authorship

I hereby declare that the thesis submitted is my own unaided work. All direct or indirect sources used are acknowledged as references. This thesis was not previously presented to another examination board and has not been published.

Selbständigkeitserklärung

Ich erkläre hiermit, dass ich die vorliegende Arbeit selbständig verfasst und nur unter Verwendung der angegebenen Quellen und Hilfsmittel angefertigt habe. Die Arbeit wurde weder einer anderen Prüfungsbehörde vorgelegt noch veröffentlicht.

Hamburg, den 19. September 2018 .....

The work in this thesis was supported by Fraunhofer Institute for Silicon Technology, Application Center Power Electronics for Renewable Energy Systems. Their cooperation is hereby gratefully acknowledged.

Abstract

Power electronics are widely-used in nearly every industrial and domestic sector and an important component for the integration of renewable energy systems into the electrical grid. Their increasing share comes along with power quality issues, that need to be addressed to ensure a safe and efficient electric power supply. Active power filters provide reactive power and harmonic compensation in order to reduce losses and to improve the overall power quality of the grid. While proven techniques for the design and control of active power filters exist, the availability of higher computational power enables the examination of more advanced control methods. This thesis enhances the novel linear state signal shaping model predictive control scheme to facilitate this method for harmonic compensation. For this purpose, new approaches for amplitude control are presented and a performance comparison with a classical active power filter is conducted with simulations. Results show, that the new controller not only matches up to the performance of the classical concept, but is also able to adjust to load changes.

Zusammenfassung

Leistungselektronik ist in nahezu jedem industriellen und privaten Sektor zu finden und zudem ein wichtiger Bestandteil, um regenerative Energiequellen in das elektrische Versorgungsnetz einzubinden. Mit der zunehmenden Zahl leistungselektronischer Komponenten steigen die Anforderungen an die Netzqualität, um eine sichere und effiziente elektrische Energieversorgung sicherstellen zu können. Aktive Netzleistungsfilter stellen Blindleistungs- und Oberwellenkompensation bereit, um die Netzqualität anzuheben und Energieverluste zu minimieren. Es existieren zwar ausgereifte Methoden, um aktive Netzleistungsfilter zu entwerfen und um sie zu regeln, die Verfügbarkeit von leistungsfähigen Computern ermöglicht es jedoch, komplexere Regelungstechniken zu erproben. Diese Arbeit erweitert einen neuartigen modellprädiktiven Regler, um ihn für Oberwellenkompensation einsetzen zu können. Zu diesem Zweck wird ein neuer Ansatz zur Amplitudenstabilisierung vorgestellt und ein Vergleich der Methode mit einem klassischen Konzept zur Oberwellenkompensation wird mit Hilfe von Simulationen durchgeführt. Die Ergebnisse zeigen, dass der neuartige Regler nicht nur dieselbe Leistungsfähigkeit besitzt wie der klassische Ansatz, sondern zudem noch flexibel gegenüber Laständerungen ist.

Table of Contents

List of Figures

List of Tables

Acknowledgements

I would like to thank my supervisors Prof. Dr.-Ing. Florian Wenck and Prof. Dr.-Ing. Gerwald Lichtenberg for their support and guidance during the work of this thesis and writing this thesis. In addition I like to thank Prof. Dr. Frerk Haase for giving me the opportunity to work at the Fraunhofer ISIT Application Center Power Electronics for Renewable Energy Systems, providing the necessary resources and financial aid during this time.

I would like to express my appreciation to my daily supervisor Carlos Cateriano Yáñez for his constant feedback and discussions both at work and even after working hours. Dr.-Ing. Georg Pangalos also provided me with comments and valuable resources during the writing of this thesis, for which I am deeply grateful.

Hamburg,
September 19, 2018

Kathrin Weihe

Chapter 1

Introduction

The work done in the scope of this thesis is part of the project Norddeutsche EnergieWende (NEW) 4.0, which evaluates possibilities of how to ensure a safe, cost-efficient and environmentally compatible energy supply based solely on renewable energy sources by the end of 2035, [1]. This thesis particularly addresses how to improve power quality on distribution grid level by means of a novel control scheme.

To introduce the work of this thesis, a short description of the concept of quality in power networks is given, followed by an overview of state of the art techniques and research goals, concluded by an outline.

1-1 Motivation

In order to maintain generation, transmission and distribution, the term power quality (PQ) generally is used to assess the condition of electric power in the grid. Pollution of electric power can be categorised either into natural or unpredictable causes like weather conditions, lightning and equipment failure, or into causes related to loads such as fluorescent lamps, adjustable speed drives, consumer electronic devices and solid-state switching converters. Natural causes often lead to transient problems such as voltage swells, sags and short duration variations as well as power frequency variations, while load-caused problems tend to show steady state influences on the PQ such as long duration voltage variations, flicker, waveform distortions, poor power factor and unbalanced voltages, [2].

Waveform distortions and harmonics in particular are of special interest in low voltage distribution grids since customer loads are main sources of harmonic pollution. Har-

monics are sinusoidal currents or voltages with a frequency of integer multiples of the signal's fundamental frequency. Due to their nonlinear load characteristics, power electronic devices such as consumer electronics using switch-mode power supplies, as well as inverters which are used along with photovoltaic (PV) systems to connect them to the distribution grid draw harmonic currents which cause voltage distortions as they interact with the grid. Some undesirable effects of harmonic pollution are additional energy losses of power capacitors and transformers, vibrations in electrical machines and malfunction of control devices, [3].

In Germany, the DIN EN 50160 standard lists characteristics for the quality of the electric grid to ensure the security of energy supply, [4]. While electric utility companies are bound to follow this norm, operators of harmonic sources are also compelled to keep disturbances within permissible limits. The standard EN 61000-3-2 defines harmonic thresholds for nonlinear loads connected to the public network, [5].

Mitigation techniques are needed to keep harmonic pollution within bounds. Solutions classically consist of designing passive components such as line transformers and capacitor banks to filter out specific harmonics. Advances in power electronics and computational power lead to more sophisticated approaches in the form of active power filters (APF), which can handle more than one harmonic at a time and ideally are capable of mitigating other PQ issues such as poor power factor [6].

Since wind turbine and PV systems extensively rely on power electronic devices for generation, transmission and storage of power to make these weather-based systems controllable and integrable, the demand for harmonic compensation techniques will increase, [7]. This thesis contributes to the NEW 4.0 project by exploring new methods to achieve harmonic compensation.

1-2 State of the Art

For harmonic compensation and power factor correction proven technologies exist, they are commonly divided into passive power filter and APF approaches, with APF more broadly researched, since they allow for a wider application range. Trends in the field of APF tend towards improving the efficiency, [8], and developing adaptive control techniques to be able to adjust to load changes more flexibly, [9]. Hybrid APF, consisting of both active and passive filter components, are a common research topic due to their potential to greatly decrease the cost of the filter, [10, 11].

Publications on the use of model predictive control (MPC) in combination with APF are scarce and mostly not more than two years old at the time this thesis is being written, [12, 13, 14, 15]. This is mainly owed to the computational requirements of MPC. Power electronic devices need fast controllers, but MPC-based methods require a higher

computational effort than conventional controllers, [16]. In recent years, the availability of more powerful embedded computers increased and computationally efficient algorithms to solve the MPC optimization problem emerged, [17, 18, 19], enabling the use of MPC in power electronics, [20].

The research field of MPC is huge in general, many different variants exist, which evolved from the original linear MPC concept of the 1970s. A recently developed novel linear state signal shaping (LSSS) MPC concept incorporates signal shapes into the cost function instead of evaluating a reference tracking error, which shows promising properties to be used as controller in power electronics [21, 22]. Since this method is so recent, it still faces some problems, which this thesis aims to help overcome.

1-3 Research Goals

Current work on the LSSS MPC scheme shows, that this method has the capability of ensuring a sinusoidal waveform of the controlled plant states. However, this approach is not able to control the amplitude of the state signal, which is an important requirement especially regarding applications for power quality improvement. In addition, first simulations using the LSSS MPC approach indicates that this control method could be facilitated for harmonic compensation in the grid, but the performance compared to existing APF techniques is not yet evaluated. Based on this preconditions, the main research goals of this thesis are as followed:

- Develop a numerically efficient method to ensure that the amplitude magnitude of controlled plant states does not increase above a certain limit.
- Determine a way to set the amplitude magnitude to a defined value.
- Compare the performance of harmonic compensation by the LSSS MPC approach with an established APF technique.

1-4 Structure of the Thesis

The content of this thesis is organised into the following chapters:

Chapter 2 gives an overview on existing methods for harmonic mitigation with a focus on APF and their control techniques. Numerous methods regarding reference signal estimation for APF exist, therefore only two of the most commonly applied approaches are introduced to keep the chapter confined.

Chapter 3 lays out the basics of MPC as well as how to modify MPC to constrain the optimization problem in different formulations. In addition, the concept of LSSS is described along with methods to include this concept into the MPC scheme.

Chapter 4 first provides an extended analysis of the numerical properties of the unconstrained LSSS MPC, followed by the description of developed methods to control the plant state amplitude along with simulation results.

Chapter 5 comprises simulations of the LSSS MPC acting as an active power filter in a three phase grid as well as a comparison of a classical APF with the LSSS MPC approach.

Chapter 6 concludes this thesis with a summary of the results and an outlook on future work.

Chapter 2

Classic Control Approaches for Active Power Filters

A load connected to a perfectly sinusoidal alternating current (AC) supply voltage, where the supply waveform only consists of a fundamental frequency, can be characterised as nonlinear load, if the load current drawn from the supply voltage shows characteristic or noncharacteristic harmonics or fluctuating currents, [2]. Most grid connected loads at least to some extent show nonlinear characteristics, although power electronic converters play a prominent role in the class of these loads, since their amount of produced harmonic currents is quite high. Power electronic converters are used for voltage conversion, when electrical direct current (DC) voltage is needed for operation, which is the case for nearly every modern consumer device that uses semiconductor technology like personal computers and smartphones. Even for electrical machines that innately use AC supply voltage, power electronics are applied more and more to adjust the supply frequency for advanced control techniques. When electric energy is not generated by a power plant's rotating synchronous machine, but e.g. by a photovoltaic (PV) system or a wind turbine, these generators need to be synchronised to the grid by power electronic devices. Hence the change of the electric grid towards distributed generation, fast advancements in research and good availability of power electronics lead to an ever increasing share of these loads in the modern grid and the trend does seem to last, [23]. Since harmonics negatively influence the power quality (PQ) of the grid as outlined in section 1-1, the topic of harmonic mitigation is an active research topic, [24].

In order to properly asses the quality of newly developed methods for harmonic compensation compared to classical compensation methods, this chapter gives an introduction to existing methods with a focus on active power filters (APF) and their con-

trol techniques. After a short overview on common harmonic mitigation techniques in section 2-1, two predominantly used reference signal estimation techniques are introduced in section 2-2 followed by a description of common control techniques for APF in section 2-3.

2-1 Overview

Since its inception, the AC voltage supply system relies on passive components, namely capacitors and inductances, as filters to cope with various effects like improving steady state and dynamic voltage and phase stabilities. Harmonic distortion can also be suppressed with passive filtering by laying out a combination of specifically designed inductances, resistances and capacitors to block AC currents above a certain cut-off frequency. While this approach is simple and inexpensive, the designed filters are heavily dependent on the power system and the load they are connected to, [25]. Furthermore, they are of large size, can cause resonance, and tolerances in components make it difficult to tune the filters to exactly meet the design requirements. Due to those disadvantages and as regulations become more and more strict, passive filters tend to get replaced by APFs, which are discussed in this section.

2-1-1 Measures for Harmonic Distortion

Main sources for definition and measures of harmonics are the IEEE Standard 1459 and the IEC Standard 61000-1-1, [26, 27]. As outlined in these standards, periodic nonsinusoidal waveforms can be described by Fourier analysis. Considering the frequencies of harmonics are integer multiples of the fundamental frequency, nonsinusoidal currents are described as

$$\begin{aligned} i(t) &= I_{DC} + \sum_{h=1}^{N} I^{(h)} \cos(h\omega_0 t + \phi_h) \\ &= I_{DC} + i^{(1)}(t) + i^{(2)}(t) + i^{(3)}(t) + \dots \ , \end{aligned} \tag{2-1}$$

where I_{DC} denotes a DC current offset, ω_0 denotes the fundamental frequency and $I^{(h)}$ and ϕ_h denote the root mean square (RMS) current and phase shift respectively for the hth harmonic. When negative and positive half-waves of a waveform are symmetrical, the Fourier series only contains odd harmonics. This is typically the case with currents drawn from nonlinear loads in power systems, such as rectifiers and other voltage source converters.

Figure 2-1 shows the typical current drawn from a rectifier. The plot on the left shows the waveform, the plot on the right shows the frequency domain spectrum. As can be seen, only odd harmonics contribute to the signal.

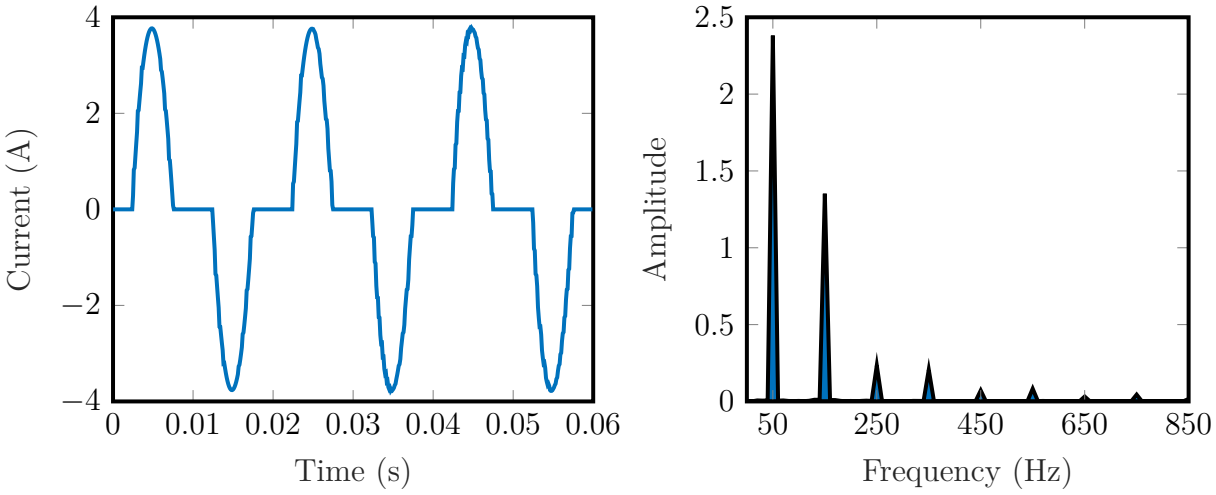

Figure 2-1: Current drawn from a rectifier with the signal shown in time domain and frequency domain.

The amount of harmonics contained in a waveform can be indicated by the total harmonic distortion (THD), which is defined as the relationship between the RMS value of the current harmonics and the RMS value of the fundamental current expressed in percentage as

$$\mathrm{THD} = \frac{\sqrt{\sum_{h=2}^{\infty} \left(I^{(h)}\right)^2}}{I^{(1)}} \cdot 100\,\% \,. \tag{2-2}$$

Often the THD is truncated at a frequency of around 1.6 kHz due to the limited bandwidth of current measurement devices. Being easily calculated, the THD is a common metric to express, how distorted a current waveform is. The THD for the current drawn by the rectifier in figure 2-1 is 58.5 %.

2-1-2 Active Harmonic Compensation Techniques

Active power filters compensate harmonic currents by extracting the harmonic content and inducing the exact negative of this waveform into a coupling point. This way, the harmonic currents are cancelled out and only the fundamental current remains. Figure 2-2 shows the general structure of an APF. The filter is coupled to supply system and load either with inductances or a transformer depending on its topology. Information regarding the amount of harmonic distorted currents are acquired with

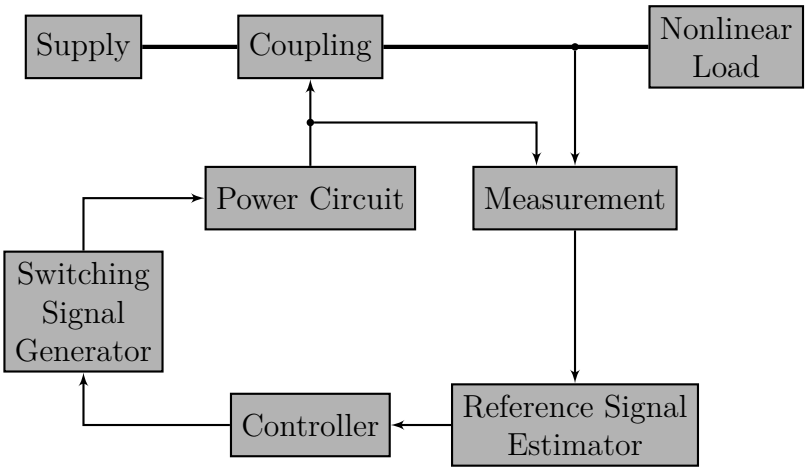

Figure 2-2: Block diagram of the generalised structure of an acitve power filter.

measurements in order to generate a reference signal that is able to cancel out harmonics. The inverted harmonic currents are induced into the coupling point by a power circuit, most commonly a switching-mode voltage source converter (VSC). A controller ensures, that the VSC induces the correct waveform into the grid by calculating the control input, which minimizes the error between reference and output of the VSC. The switching signals itself are generated by a switching signal generator based on the calculated control input.

Two different configurations exist for APF, namely series APF and shunt APF. Series APF as shown in figure 2-3 are coupled to the grid through a transformer, injecting a compensating voltage v_c across the transformer into the coupling point, so that the feeder line current i_f maintains a sinusoidal waveform when the distorted current i_l is drawn from the grid. The transformer can be seen as dynamic impedance, where for harmonic currents the impedance is high, but for the fundamental current the impedance

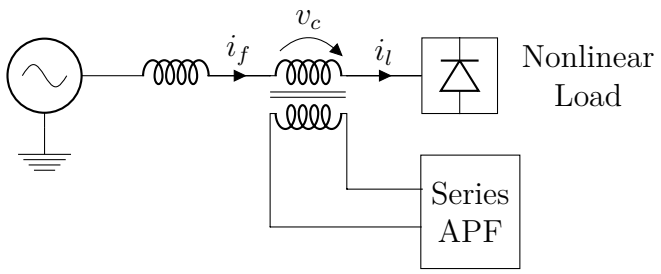

Figure 2-3: Acitve power filter in series configuration.

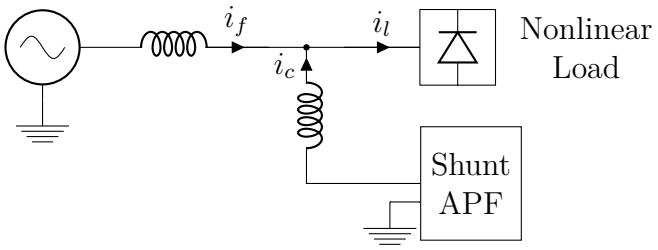

Figure 2-4: Acitve power filter in shunt configuration.

is zero, therefore only the fundamental current is allowed to pass.

Shunt APF on the other hand are coupled with an inductance, they are connected parallel to the nonlinear load. The compensation current i_c generated by the shunt APF is injected into the coupling point and the harmonic currents are cancelled out, leaving only the fundamental current. The structure of the shunt APF is shown in figure 2-4. This configuration is more widely used than the series APF, considering only the negative equivalent of the harmonic currents are carried on the lines leading to the coupling point, while much higher currents on the secondary side of the series APF coupling transformer are needed to produce the equivalent harmonic voltages, leading to power losses, [24].

In addition to this two configurations, numerous variations of hybrid APF exist, consisting of combinations of both series and shunt APF or additional passive filter components, [2, 6].

Although APF are able to provide good harmonic compensation without being dependent on the power system they are connected to like passive filters are, they still need to be designed according to the loads they are supposed to compensate, [28]. The main reason for this is, that reference current estimation techniques often still rely on high pass or low pass filters, as will be shown in the following section.

2-2 Reference Signal Estimation

In order to achieve good harmonic compensation results, estimating the reference signal is essential when operating an APF. While various techniques exist for this part, the two most common methods are introduced in this section. For the benefit of conciseness, only methods for the operation of the more widely used shunt APF are described.

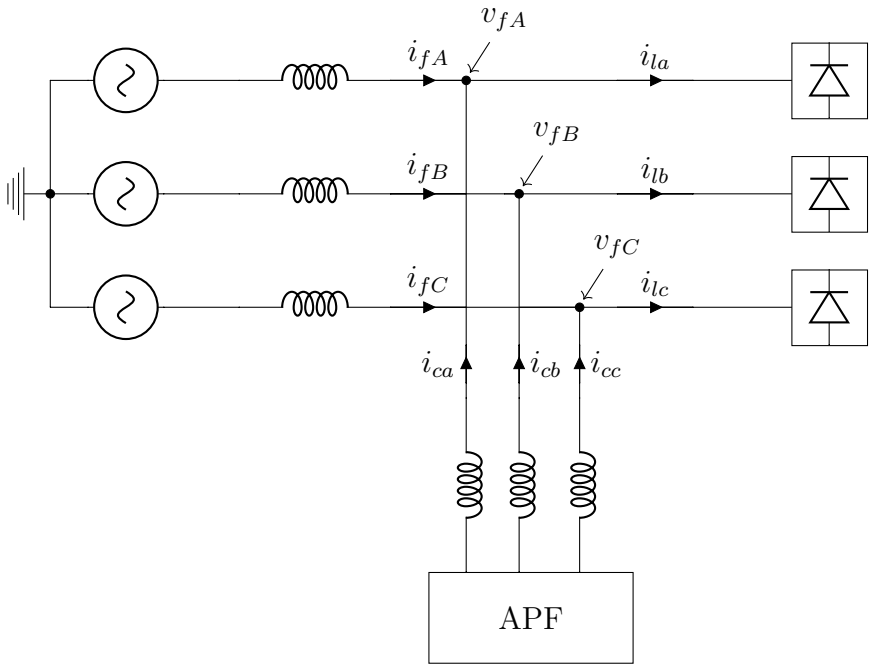

Figure 2-5: Three-phase three-node grid model.

2-2-1 Instantaneous Reactive Power Theory

Considering a three phase three node grid as shown in figure 2-5, the reference signal for the operation of a shunt APF can be obtained by applying the instantaneous reactive power (IRP) theory, [29]. Assuming a balanced three-phase supply voltage, with the instantaneous voltages v_{fA}, v_{fB} and v_{fC} at the point of common coupling (PCC), as well as the instantaneous load currents i_{lA}, i_{lB} and i_{lC}, the Clarke transformation

$$\begin{pmatrix} v_\alpha \\ v_\beta \end{pmatrix} = \sqrt{\frac{2}{3}} \begin{pmatrix} 1 & -\frac{1}{2} & -\frac{1}{2} \\ 0 & \frac{\sqrt{3}}{2} & -\frac{\sqrt{3}}{2} \end{pmatrix} \begin{pmatrix} v_{fA} \\ v_{fB} \\ v_{fC} \end{pmatrix} , \tag{2-3}$$

$$\begin{pmatrix} i_{l\alpha} \\ i_{l\beta} \end{pmatrix} = \sqrt{\frac{2}{3}} \begin{pmatrix} 1 & -\frac{1}{2} & -\frac{1}{2} \\ 0 & \frac{\sqrt{3}}{2} & -\frac{\sqrt{3}}{2} \end{pmatrix} \begin{pmatrix} i_{lA} \\ i_{lB} \\ i_{lC} \end{pmatrix} , \tag{2-4}$$

transfers the instantaneous voltages and currents to the $\alpha\beta$-frame. With this transformation, the space vector of three phase voltages or currents is projected onto a two dimensional plane. When choosing the complex plane for this, the real axis is called α axis, corresponding to active or real currents and voltages, and the imaginary axis is called β axis, corresponding to reactive or imaginary currents and voltages. The

instantaneous real power p_l and instantaneous imaginary power q_l then are calculated by

$$\begin{pmatrix} p_l \\ q_l \end{pmatrix} = \begin{pmatrix} v_\alpha & v_\beta \\ -v_\beta & v_\alpha \end{pmatrix} \begin{pmatrix} i_{l\alpha} \\ i_{l\beta} \end{pmatrix}. \tag{2-5}$$

The instantaneous real power p_l represents the instantaneous total energy flow per time unit between load and supply, while the imaginary power q_l quantifies the energy that is exchanged between the three phases, which does not contribute to the exchanged energy between load and supply.

With the help of a high pass filter, the undesired harmonic contents of p_l can be extracted to obtain $\tilde{p}_l$, which contains only the instantaneous harmonics. From this the $\alpha\beta$-currents

$$\begin{pmatrix} i_{l\alpha} \\ i_{l\beta} \end{pmatrix} = \frac{1}{v_\alpha^2 + v_\beta^2} \begin{pmatrix} v_\alpha & -v_\beta \\ v_\beta & v_\alpha \end{pmatrix} \begin{pmatrix} -\tilde{p}_l \\ -\tilde{q}_l \end{pmatrix}, \tag{2-6}$$

are calculated with negative signs for $\tilde{p}_l$ and $\tilde{p}_l$, since the inverse of the harmonic content has to be induced into the grid for compensation. Lastly the inverse Clarke transformation is applied to obtain the reference currents for each phase.

This method can be extended to additionally provide reactive power compensation and voltage stabilization by calculating the power losses in the grid-coupled VSC, which induces the reference currents into the PCC. In general, VSC consist of a DC link capacitor that is used as energy storage. With a fixed supply voltage, this storage is constantly discharged and charged to an equal amount in order to be able to output an arbitrary current waveform. When the PCC supply voltage drops, the DC link capacitor needs to be charged more often than it is discharged in order to maintain its capacitor voltage and hence its energy supply. Considering p_{loss} as active power, that is needed to keep the DC link capacitor voltage at a reference voltage, with

$$\tilde{p}_l^\star = \tilde{p}_l + p_{loss}\,, \tag{2-7}$$

where $\tilde{p}_l^\star$ denotes the instantaneous real power including losses due to a decreased voltage at the coupling point, a reference current can be calculated using equation (2-6) and the inverse Clarke transformation to obtain simultaneous harmonic compensation and PCC voltage compensation. The calculation of p_{loss} is a nonlinear problem, but around the set point it can be estimated as

$$p_{loss} \approx K_p\, e_{DC}(t) + K_i \int_0^{T_d} e_{DC}(t)\,\mathrm{d}t\,, \tag{2-8}$$

where e_{DC} denotes the error between the DC link reference capacitor voltage and the actual capacitor voltage, and K_p and K_i denote parameters, which are chosen in such

a way, that in a given time T_d the power p_{loss} is estimated to a sufficiently accurate value. The parameters can be chosen either by analysing the relationship between DC link capacitor voltage error and p_{loss} of the VSC or by closed-loop tuning methods like the Ziegler-Nichols method, [30]. A drawback of this additional voltage stabilization technique is the requirement to design the APF according to a given load, since the reference DC link voltage has to be adjusted to the assumed voltage drop at the coupling point.

2-2-2 Synchronous Reference Frame Theory

The synchronous reference frame (SRF) control method also uses the Clarke transformation to project the rotating three phase space vector onto the complex plane. Additional to this, the Park transformation

$$\begin{pmatrix} i_d \\ i_q \end{pmatrix} = \begin{pmatrix} \cos(\theta) & \sin(\theta) \\ -\sin(\theta) & \cos(\theta) \end{pmatrix} \begin{pmatrix} i_{l\alpha} \\ i_{l\beta} \end{pmatrix} , \tag{2-9}$$

is applied, where the active current i_d and reactive current i_q are rotating along with the instantaneous currents $i_{l\alpha}$ and $i_{l\beta}$ with the same angular speed. They are synchronized to each other with the angle θ. If no harmonics are present, i_d and i_q are static DC currents. If the load current is distorted, these currents are composed as

$$i_d = I_{dDC} + i_{dAC} , \tag{2-10}$$

$$i_q = I_{qDC} + i_{qAC} , \tag{2-11}$$

where the active component I_{dDC} and the reactive component I_{qDC} denote the DC share of the currents, which coincide with the fundamental of the load current, while the harmonic load current components contribute to the oscillating currents i_{dAC} and i_{qAC}. Only the active components are of interest, therefore a low pass filter (LPF) is used to remove the oscillating currents from i_d, such that only I_{dDC} remains. The inverse Park and Clarke transformations are applied to obtain the filtered load current waveform i_{fund}, which is free of harmonics.

Figure 2-6 shows the structure of this reference signal estimation method. A phase locked loop (PLL) is used to synchronize the currents with the angle θ for the Park transformation and inverse Park transformation. The reference current is obtained by subtracting the measured load current with the fundamental current i_{fund}.

2-3 Control Techniques

Shunt APF inject the compensation current into the coupling point using switched-mode voltage source converters, therefore the reference current has to be converted into

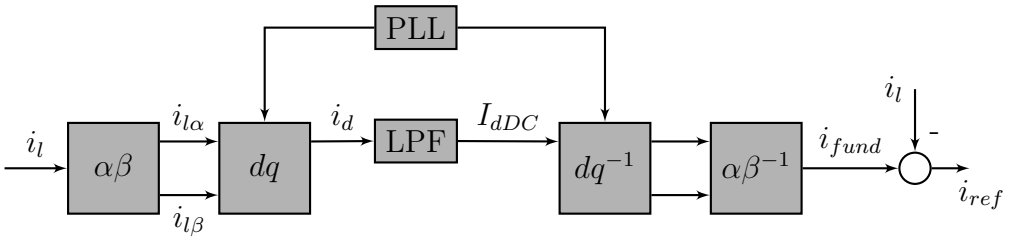

Figure 2-6: Estimating the reference signal with the SRF method. The block $\alpha\beta$ refers to the Clarke transformation, the block dq refers to the Park transformation.

appropriate binary switching signals to control the VSC. This section describes two of the most commonly applied control techniques for APF.

2-3-1 Hysteresis Control

With hysteresis control, upper and lower tolerance limits are defined, to include the reference signal in a tolerance band with a width of H. When the current output of the VSC reaches the upper tolerance limit, the switching signal is set to zero, for the output current to decrease. As long as the output current stays within the tolerance band, no switching action is taken, but when the lower limit is reached, the switching signal is set to one accordingly. In figure 2-7 this control scheme is shown. To obtain currents with small switching ripples, smaller values of H can be chosen. While this controller is simple in design and provides small reference errors with appropriate tolerance bands, the main drawback of this scheme is a variable switching frequency, which could lead to unwanted resonances.

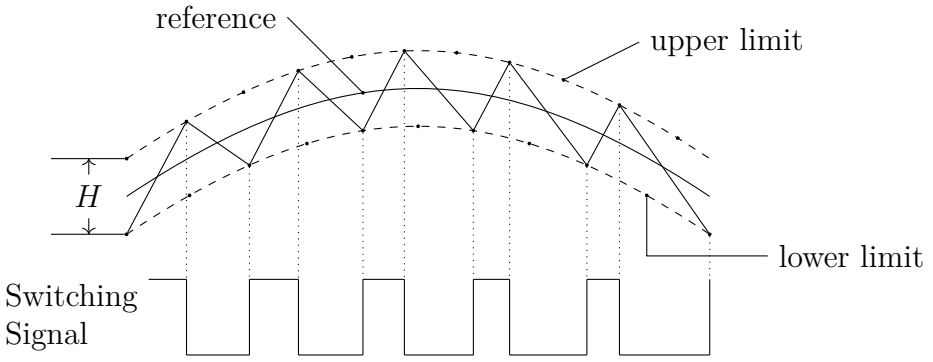

Figure 2-7: Hysteresis control scheme showing the tolerance band and the resulting switching signals.

2-3-2 Linear Control

In the linear control scheme, the reference current is compared to the output current of the VSC. Based on the tracking error, a PI controller calculates the control signal, where the PI controller parameters commonly are derived using Bode plot analysis and frequency domain design. The control signal is compared to a sawtooth waveform in a pulse width modulation (PWM) generator to supply the switching signal for the VSC. Figure 2-8 depicts the linear control scheme. The switching frequency of this control technique is constant, since it is established by the repetitive sawtooth signal, which is an advantage compared to hysteresis control.

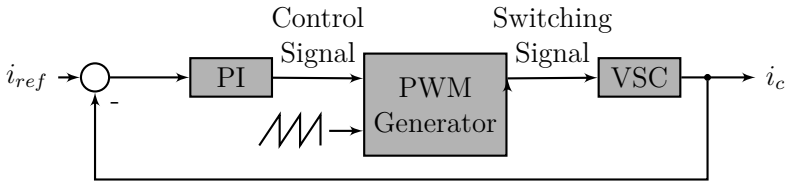

Figure 2-8: Linear control scheme.

Chapter 3

Model Predictive Control

Model predictive control (MPC) is a multivariable control technique which is inherently able to handle systems with physical or actuator limitations. An internal model is used to predict the future system behviour and calculate the optimal input to the plant to achieve the control goal. Since its first implementations in the 1970s, MPC has become a widely used control technique for various applications. Due to the higher computational effort compared to classic control strategies, first approaches used heuristic methods to control plants in slow industrial processes, [31]. The rapid increase in computational power and good availability of low-cost embedded systems nowadays enables the implementation of MPC even on fast paced processes such as controlling power converters with computation times of as little as a few microseconds, [20].

This chapter gives a brief introduction to the concept of model-based prediction and the formulation of the optimization problem which is used to compute the optimal control action. In addition, the concept of linear state signal shaping (LSSS) is introduced, as well as how this concept can be utilized to formulate a novel MPC control scheme. This chapter is concluded with assumptions for both MPC and LSSS MPC. Also limitations existing when work on this thesis began are discussed.

3-1 Model-Based Prediction

Since model-based prediction plays an important role for MPC, this sections outlines the basics of both discrete-time state space models and prediction in preparation for the more advanced concepts used in later sections. Regarding the notation, $\mathbf{0}^{a\times a}$ denotes a zero matrix with the dimension $a \times a$, $\mathbf{0}$ denotes a zero submatrix with appropriate

dimensions to complete a matrix, $\mathbf{I}^a$ denotes a unity matrix with the dimension $a \times a$ and $\mathbf{I}$ analogously denotes a unity submatrix with appropriate dimensions to complete a matrix. For further usage $n \in \mathbb{N}$ denotes the number of states, $m \in \mathbb{N}$ denotes the number of inputs, $p \in \mathbb{N}$ denotes the number of outputs and $d \in \mathbb{N}$ denotes the number of disturbances. The symbol $\otimes$ denotes the Kronecker product and $\mathbf{M}^\dagger$ indicates the pseudoinverse of the matrix $\mathbf{M}$.

3-1-1 State Space Model

Any dynamic time-invariant system behaviour can be represented by a mathematical model

$$\dot{\mathbf{x}}(t) = f\left(\mathbf{x}(t), \mathbf{u}(t)\right) \tag{3-1}$$
$$\mathbf{y}(t) = g\left(\mathbf{x}(t), \mathbf{u}(t)\right) \tag{3-2}$$
$$\mathbf{x}(0) = \mathbf{x}_0, \tag{3-3}$$

with the time t, and where $\mathbf{x} \in \mathbb{R}^n$ refers to the state vector, $\mathbf{u} \in \mathbb{R}^m$ refers to the input vector, $\mathbf{y} \in \mathbb{R}^p$ refers to the output vector, $f : \mathbb{R}^n \times \mathbb{R}^m \to \mathbb{R}^n$ is called state equation and $g : \mathbb{R}^n \times \mathbb{R}^m \to \mathbb{R}^p$ is called output equation and $\mathbf{x}_0$ is the inital state. If f is linear in $\mathbf{x}$ and $\mathbf{u}$, the state equation (3-1) can be represented by

$$\dot{\mathbf{x}}(t) = \tilde{\mathbf{A}}\mathbf{x}(t) + \tilde{\mathbf{B}}\mathbf{u}(t)\ , \tag{3-4}$$

with the system matrix $\tilde{\mathbf{A}} \in \mathbb{R}^{n\times n}$ and the input matrix $\tilde{\mathbf{B}} \in \mathbb{R}^{n\times m}$. With a fixed sampling time T_s and samples taken at $t = kT_s$ for $k = 0, 1, 2, \ldots$, the model (3-4) can be rewritten as discrete-time state space model

$$\mathbf{x}(k+1) = \mathbf{A}\mathbf{x}(k) + \mathbf{B}\mathbf{u}(k)\ , \tag{3-5}$$

with appropriate matrices $\mathbf{A} \in \mathbb{R}^{n\times n}$ and $\mathbf{B} \in \mathbb{R}^{n\times m}$. Note that in this thesis full state measurement is assumed and only states are targeted for control, so a dedicated output equation (3-2) is not used.

Assuming that state disturbances additionally enter the system and disturbance measurements are available, model (3-5) can be modified as

$$\mathbf{x}(k+1) = \mathbf{A}\mathbf{x}(k) + \mathbf{B}\mathbf{u}(k) + \mathbf{E}\mathbf{d}_m(k)\ , \tag{3-6}$$

where $\mathbf{d}_m \in \mathbb{R}^d$ refers to the disturbance vector and $\mathbf{E} \in \mathbb{R}^{n\times d}$ to the disturbance matrix. By combining the input vector and the disturbance vector, model (3-6) can be rewritten as

$$\mathbf{x}(k+1) = \mathbf{A}\mathbf{x}(k) + \mathbf{B}_t\mathbf{u}_t(k)\ , \tag{3-7}$$

where $\mathbf{B}_t = \begin{pmatrix}\mathbf{B} & \mathbf{E}\end{pmatrix} \in \mathbb{R}^{n\times(m+d)}$ and $\mathbf{u}_t = \begin{pmatrix}\mathbf{u}(k) & \mathbf{d}_m(k)\end{pmatrix}^\mathsf{T} \in \mathbb{R}^{m+d}$. This way the discrete-time state space model can be treated in the same manner as a model without state disturbances. To be able to differentiate between controllable inputs and disturbances, notation (3-6) mainly is used in this thesis.

3-1-2 Prediction

Provided that the future control trajectory is known or can be estimated, the undisturbed system behaviour over a finite future horizon H_p starting at the sampling instant k with known or measured initial state $\mathbf{x}(k)$ can be predicted by

$$\mathcal{X}(k) = \Psi\mathbf{x}(k) + \Phi\mathcal{U}(k)\ , \tag{3-8}$$

and with

$$\boldsymbol{\Psi} = \begin{pmatrix}\mathbf{A}\\ \mathbf{A}^2\\ \mathbf{A}^3\\ \vdots\\ \mathbf{A}^{H_p}\end{pmatrix}, \quad \boldsymbol{\Phi} = \begin{pmatrix}\mathbf{B} & \mathbf{0} & \mathbf{0} & \cdots & \mathbf{0}\\ \mathbf{AB} & \mathbf{B} & \mathbf{0} & \cdots & \mathbf{0}\\ \mathbf{A}^2\mathbf{B} & \mathbf{AB} & \mathbf{B} & \cdots & \mathbf{0}\\ \vdots & \vdots & \vdots & \ddots & \\ \mathbf{A}^{H_p-1}\mathbf{B} & \mathbf{A}^{H_p-2}\mathbf{B} & \mathbf{A}^{H_p-3}\mathbf{B} & \cdots & \mathbf{B}\end{pmatrix}, \tag{3-9}$$

where $\mathcal{X}(k) = \begin{pmatrix}\mathbf{x}(k+1) & \mathbf{x}(k+2) & \cdots & \mathbf{x}(k+H_p)\end{pmatrix}^\mathsf{T} \in \mathbb{R}^{nH_p}$ denotes the vector of future states, $\mathcal{U}(k) = \begin{pmatrix}\mathbf{u}(k) & \mathbf{u}(k+1) & \cdots & \mathbf{u}(k+H_p-1)\end{pmatrix}^\mathsf{T} \in \mathbb{R}^{mHp}$ denotes the vector of future inputs, and with the prediction matrices $\Psi \in \mathbb{R}^{nH_p\times n}$ and $\boldsymbol{\Phi} \in \mathbb{R}^{nH_p\times mH_p}$.

A commonly used method to facilitate prediction in MPC is to describe the vector of future states in terms of future input changes $\Delta\mathcal{U}$, with

$$\Delta\mathcal{U} = \begin{pmatrix}\Delta\mathbf{u}(k)\\ \Delta\mathbf{u}(k+1)\\ \vdots\\ \Delta\mathbf{u}(k+H_p-1)\end{pmatrix} = \begin{pmatrix}\mathbf{u}(k) & - & \mathbf{u}(k-1)\\ \mathbf{u}(k+1) & - & \mathbf{u}(k)\\ & \vdots & \\ \mathbf{u}(k+H_p-1) & - & \mathbf{u}(k+H_p-2)\end{pmatrix}. \tag{3-10}$$

For many applications it is also useful to define a control horizon H_u additionally to the prediction horizon H_p, assuming that $H_u \leq H_p$ and that $\Delta\mathbf{u}(k+i) = 0$ for $i \geq H_u$, so that $\mathbf{u}(k+i) = \mathbf{u}(k+H_u-1)$ for all $i \geq H_u$. With (3-10), the prediction stated in (3-8) can be reformulated as

$$\mathcal{X}(k) = \boldsymbol{\Psi}\mathbf{x}(k) + \boldsymbol{\Upsilon}\mathbf{u}(k-1) + \boldsymbol{\Theta}\Delta\mathcal{U}\ , \tag{3-11}$$

with

$$\boldsymbol{\Upsilon} = \begin{pmatrix} \mathbf{B} \\ \mathbf{AB} + \mathbf{B} \\ \mathbf{A}^2\mathbf{B} + \mathbf{AB} + \mathbf{B} \\ \vdots \\ \sum_{j=0}^{H_p-1} \mathbf{A}^j\mathbf{B} \end{pmatrix}, \tag{3-12}$$

$$\boldsymbol{\Theta} = \begin{pmatrix} \mathbf{B} & \mathbf{0} & \mathbf{0} & \cdots & \mathbf{0} \\ \mathbf{AB} + \mathbf{B} & \mathbf{B} & \mathbf{0} & \cdots & \mathbf{0} \\ \mathbf{A}^2\mathbf{B} + \mathbf{AB} + \mathbf{B} & \mathbf{AB} + \mathbf{B} & \mathbf{B} & \cdots & \mathbf{0} \\ \vdots & \vdots & \vdots & \ddots & \vdots \\ \sum_{j=0}^{H_p-1} \mathbf{A}^j\mathbf{B} & \sum_{j=0}^{H_p-2} \mathbf{A}^j\mathbf{B} & \cdots & \cdots & \sum_{j=0}^{H_p-H_u} \mathbf{A}^j\mathbf{B} \end{pmatrix}, \tag{3-13}$$

where $\mathbf{u}(k-1)$ denotes the last input before sampling instant k and with the prediction matrices $\boldsymbol{\Upsilon} \in \mathbb{R}^{nH_p \times m}$ and $\boldsymbol{\Theta} \in \mathbb{R}^{nH_p \times mH_p}$.

To include measured disturbances into the prediction, (3-10) can be extended as

$$\mathcal{X}(k) = \boldsymbol{\Psi}\mathbf{x}(k) + \boldsymbol{\Upsilon}\mathbf{u}(k-1) + \boldsymbol{\Theta}\Delta\mathcal{U} + \boldsymbol{\Gamma}\mathcal{D}_m \,, \tag{3-14}$$

with

$$\boldsymbol{\Gamma} = \begin{pmatrix} \mathbf{E} & \mathbf{0} & \mathbf{0} & \cdots & \mathbf{0} \\ \mathbf{AE} & \mathbf{E} & \mathbf{0} & \cdots & \mathbf{0} \\ \mathbf{A}^2\mathbf{E} & \mathbf{AE} & \mathbf{E} & \cdots & \mathbf{0} \\ \vdots & \vdots & \vdots & \ddots & \\ \mathbf{A}^{H_p-1}\mathbf{E} & \mathbf{A}^{H_p-2}\mathbf{E} & \mathbf{A}^{H_p-3}\mathbf{E} & \cdots & \mathbf{E} \end{pmatrix}, \tag{3-15}$$

where $\mathcal{D}_m = \begin{pmatrix} \mathbf{d}_m(k) & \mathbf{d}_m(k+1) & \dots \mathbf{d}_m(k+H_p-1) \end{pmatrix}^\intercal \in \mathbb{R}^{dH_p}$ denotes the vector of future measured disturbances and with the prediction matrix $\boldsymbol{\Gamma} \in \mathbb{R}^{nH_p \times dH_p}$.

3-2 Model Predictive Control as a Quadratic Programming Problem

Assuming a problem where the control goal aims to drive the states towards certain reference values, this problem can be stated in such a way, that the desired state vector is the zero vector. This can be done by transforming the state vector into an equivalent vector where the equilibrium lies at the reference. For discrete-time systems

with finite horizons, the optimal control action leading the states to the equilibrium can be obtained by the finite-horizon linear quadratic regulator (LQR), which minimizes a convex quadratic cost function

$$J(\mathbf{x}, \mathbf{u}) = \sum_{k=0}^{H_p-1} \left(\mathbf{x}(k)^\intercal \tilde{\mathbf{Q}}(k) \mathbf{x}(k) + \mathbf{u}(k)^\intercal \tilde{\mathbf{R}}(k) \mathbf{u}(k) \right) , \tag{3-16}$$

where $\tilde{\mathbf{Q}}(k) \in \mathbb{R}^{n \times n} \succeq 0$ denotes the state cost weighting matrix for all states at time step k, $\tilde{\mathbf{R}}(k) \in \mathbb{R}^{m \times m} \succ 0$ denotes the input cost weighting matrix at step k, and with $J : \mathbb{R}^n \times \mathbb{R}^m \to \mathbb{R}$. In MPC, $\tilde{\mathbf{Q}}(k)$ and $\tilde{\mathbf{R}}(k)$ are chosen to apply a weighting between the state cost and the input cost. With higher weighting on state costs, a fast state evolution towards the equilibrium will be forced by giving the input a high degree of freedom to achieve this goal. A higher weighting on input costs on the other hand will restrict the inputs, often times leading to a slower but smoother state evolution towards the equilibrium. Finding a weighting that expresses the desired trade-off for the application can be done heuristically or by using optimization methods, [32]. Since the state cost and input cost matrices are positive semidefinite and positive definite respectively, the state will be driven to the equilibrium when the cost function yields a cost of zero.

In MPC, the minimization of the LQR cost function is transformed into a quadratic program (QP)

$$\begin{aligned}
\min_{\mathbf{x},\mathbf{u}} \quad & \sum_{k=0}^{H_p-1} \left(\mathbf{x}(k)^\intercal \tilde{\mathbf{Q}}(k) \mathbf{x}(k) + \mathbf{u}(k)^\intercal \tilde{\mathbf{R}}(k) \mathbf{u}(k) \right) && \text{(3-17a)} \\
\text{subject to} \quad & \mathbf{x}(k+1) = \mathbf{A}\mathbf{x}(k) + \mathbf{B}\mathbf{u}(k) && \text{(3-17b)} \\
& \underline{\mathbf{x}} \leq \mathbf{x}(k) \leq \overline{\mathbf{x}} && \text{(3-17c)} \\
& \underline{\mathbf{u}} \leq \mathbf{u}(k) \leq \overline{\mathbf{u}} && \text{(3-17d)} \\
& \mathbf{x}(0) = \mathbf{x}_0, && \text{(3-17e)}
\end{aligned}$$

with the vectors $\underline{\mathbf{x}} \in \mathbb{R}^n$ and $\underline{\mathbf{u}} \in \mathbb{R}^m$ denoting lower state and input bounds, $\overline{\mathbf{x}} \in \mathbb{R}^n$ and $\overline{\mathbf{u}} \in \mathbb{R}^m$ denoting upper state and input bounds and $\mathbf{x}_0 \in \mathbb{R}^n$ denoting the initial state at sampling instant $k = 0$, and with $\mathbf{x}$ and $\mathbf{u}$ as decision variables to the optimization problem. It is important to note that $\mathbf{x}(k)$ and $\mathbf{u}(k)$ need to be constrained to closed convex sets containing the origin for each $k = 0, 1, \ldots$, otherwise the QP will not lead to a solution, [33].

It is possible to omit the inequality constraints on states and inputs, thus transforming the problem into a QP with equality constraints only. This type of problem often is referred to as unconstrained MPC since an analytical solution for this optimization problem exists and can be solved by the method of least squares, [34].

The current plant state needs to be measured or estimated and passed to the problem as parameter in order to solve the optimization problem. The solution consists of a future state vector as well as a future input vector containing the optimal control actions up the defined prediction horizon H_p. Instead of applying the whole input vector to the plant in a feed forward manner, a common practice for MPC is to only use the first input as control action. The receding horizon control (RHC) approach can be applied, where the new plant state is measured or estimated, the horizon is shifted one step towards the future, the solving process for the QP stated in (3-17) is repeated with the new initial state and again only the first input is applied to the plant. This way, closed loop stability and dynamic performance can be maintained while the constraints on states and inputs will still be satisfied.

In order to numerically solve the constrained problem (3-17), it needs to be formulated in a way that a solver is able to apply a suitable algorithm like the alternating direction method of multipliers (ADMM), [35], which is used in this thesis. The following sections will briefly introduce the sparse and the dense formulation, which both can be used in model predictive control, [36].

3-2-1 Sparse Formulation

Numerical solving of QP problems can be achieved by defining a new decision variable $\mathbf{z} = \begin{pmatrix}\mathbf{x} & \mathbf{u}\end{pmatrix}^\intercal \in \mathbb{R}^{H_p(n+m)+1}$ and reformulating the problem as

$$\begin{aligned} \min_{\mathbf{z}} \quad & \frac{1}{2}\mathbf{z}^\intercal \mathbf{P}\mathbf{z} && \text{(3-18a)} \\ \text{subject to} \quad & \mathbf{F}\mathbf{z} = \mathbf{c} && \text{(3-18b)} \\ & \underline{\mathbf{z}} \leq \mathbf{z} \leq \overline{\mathbf{z}}, && \text{(3-18c)} \end{aligned}$$

with appropriate matrices

$$\mathbf{Q} = \begin{pmatrix} \tilde{\mathbf{Q}}(1) & \cdots & \mathbf{0} \\ \vdots & \ddots & \vdots \\ \mathbf{0} & \cdots & \tilde{\mathbf{Q}}(H_p) \end{pmatrix}, \tag{3-19}$$

$$\mathbf{R} = \begin{pmatrix} \tilde{\mathbf{R}}(1) & \cdots & \mathbf{0} \\ \vdots & \ddots & \vdots \\ \mathbf{0} & \cdots & \tilde{\mathbf{R}}(H_u) \end{pmatrix}, \tag{3-20}$$

$$\mathbf{P} = \begin{pmatrix} \mathbf{0}^{n\times n} & \mathbf{0} & \mathbf{0} \\ \mathbf{0} & \mathbf{Q} & \mathbf{0} \\ \mathbf{0} & \mathbf{0} & \mathbf{R} \end{pmatrix}, \tag{3-21}$$

$$\mathbf{F} = \begin{pmatrix} \hat{\mathbf{A}} & \hat{\mathbf{B}} \end{pmatrix} \text{ with } \hat{\mathbf{A}} = \begin{pmatrix} -\mathbf{I}^n & \mathbf{0} & \mathbf{0} & \mathbf{0} \\ \mathbf{A} & -\mathbf{I} & \mathbf{0} & \mathbf{0} \\ \mathbf{0} & \mathbf{A} & -\mathbf{I} & \mathbf{0} \\ \mathbf{0} & \mathbf{0} & \mathbf{0} & \ddots \end{pmatrix}, \hat{\mathbf{B}} = \begin{pmatrix} \mathbf{0}^{1\times H_p} \\ \mathbf{I}^{H_p} \end{pmatrix} \otimes \mathbf{B}\,, \quad (3\text{-}22)$$

and vector

$$\mathbf{c} = \begin{pmatrix} -\mathbf{A}\mathbf{x}_0 \\ \mathbf{0} \\ \mathbf{0} \\ \vdots \end{pmatrix}, \quad (3\text{-}23)$$

where $\underline{\mathbf{z}} \in \mathbb{R}^{H_p(n+m)+1}$ denotes the lower bound and $\overline{\mathbf{z}} \in \mathbb{R}^{H_p(n+m)+1}$ denotes the upper bound of the decision variable vector and with the matrix $\mathbf{P}$ denoting the Hessian of the optimization problem.

The decision variables in sparse notations contain both future states and optimal inputs, thus the degree of freedom for the optimization problem is $n_z = H_p(n+m)$, computational effort and memory usage grows linear with respect to the prediction horizon. Due to this property and the numerically exploitable sparse pattern of the Hessian, sparse MPC formulations are assumed to perform better with long prediction horizons and a relatively small number of states, [37].

3-2-2 Condensed Formulation

Using prediction as outlined in section (3-1-2), the future states can be eliminated from the decision variables by formulating them as function of future inputs and the initial state, [34]. When also control input changes instead of control inputs are used, problem (3-17) can be formulated as

$$\min_{\mathbf{\Delta}\mathcal{U}} \quad \frac{1}{2}\Delta\mathcal{U}(k)\mathbf{P}\Delta\mathcal{U}(k) + \mathbf{q}^\intercal\Delta\mathcal{U}(k) \quad (3\text{-}24a)$$

$$\text{subject to} \quad \mathbf{l} \leq \mathbf{\Theta}\Delta\mathcal{U}(k) \leq \mathbf{o}\,, \quad (3\text{-}24b)$$

where $\mathbf{l} \in \mathbb{R}^{nH_p}$ denotes the lower bound of the inequality and $\mathbf{o} \in \mathbb{R}^{nH_p}$ denotes the upper bound of the inequality, and with

$$\mathbf{P} = \mathbf{\Theta}^\intercal\mathbf{Q}\mathbf{\Theta} + \mathbf{R}, \quad (3\text{-}25)$$

$$\mathbf{q} = -2\mathbf{\Theta}^\intercal\mathbf{Q}(\mathbf{\Psi}\mathbf{x}(k) + \mathbf{\Upsilon}\mathbf{u}(k-1)), \quad (3\text{-}26)$$

where the Hessian $\mathbf{P}$ as well as $\mathbf{q}$ can be derived by transforming (3-16) into

$$J(\Delta\mathcal{U}) = \mathcal{X}(k)^\intercal\mathbf{Q}\mathcal{X}(k) + \Delta\mathcal{U}(k)^\intercal\mathbf{R}\Delta\mathcal{U}(k) \quad (3\text{-}27)$$

and in this new cost function (3-27) replacing the state prediction vector $\mathcal{X}(k)$ according to (3-11). It is worth noting that in this formulation no equality constraint is stated, which is the implicit result of eliminating future states from the optimization problem. From this formulation it is also more obvious to see why solving the optimization problem without inequality constraints is referred to as unconstrained MPC.

In formulation (3-49) the Hessian does not contain any zero entries which leads to a dense QP. Compared to the sparse problem formulation, the number of decision variables is reduced to $n_{\Delta U} = H_p n$, resulting in a lower dimensional optimization problem. However, when inequality constraints are applied, the requirements regarding computational power and memory grow cubic with the prediction horizon in contrast to the linear growth of the sparse notation, [38]. Therefore the condensed problem formulation is more suitable for applications with smaller prediction horizons.

The structure of the Hessian can also be exploited by utilizing the Cholesky decomposition to gain a numerical advantage. This is especially important when using a solver that needs to calculate the inverse of the Hessian or when an unconstrained MPC problem is stated. Since the decomposition often times leads to lower condition numbers of the Hessian, the calculation of the optimal input is more robust against parameter changes when using the decomposed Hessian, [34]. By applying the Cholesky decomposition, the problem (3-49) can be transformed into a so called *square-root* form with

$$\mathbf{P} = \begin{pmatrix} \mathbf{S}_Q \mathbf{\Theta} \\ \mathbf{S}_R \end{pmatrix}^\mathsf{T} \begin{pmatrix} \mathbf{S}_Q \mathbf{\Theta} \\ \mathbf{S}_R \end{pmatrix}, \tag{3-28}$$

$$\mathbf{q} = -2 \begin{pmatrix} \mathbf{S}_Q (\mathbf{\Psi} \mathbf{x}(k) + \mathbf{\Upsilon} \mathbf{u}(k-1)) \\ \mathbf{0} \end{pmatrix}^\mathsf{T} \begin{pmatrix} \mathbf{S}_Q \mathbf{\Theta} \\ \mathbf{S}_R \end{pmatrix}, \tag{3-29}$$

where $\mathbf{S}_Q$ denotes an upper triangular matrix satisfying the decomposition $\mathbf{S}_Q^\mathsf{T} \mathbf{S}_Q = \mathbf{Q}$ and $\mathbf{S}_R$ denotes an upper triangular matrix satisfying the equation $\mathbf{S}_R^\mathsf{T} \mathbf{S}_R = \mathbf{R}$.

3-3 Linear State Signal Shaping

The MPC introduced in section (3-2) is posed as a regulator problem driving the states towards an equilibrium when they currently are not at an equilibrium, thus counteracting effects of any disturbances. Another commonly used control technique is the tracking method, where the control goal is that the output follows a reference signal as closely as possible. This section introduces an additional approach, where the states are not manipulated to follow a fixed reference trajectory, but instead should maintain a determined signal shape. In this linear state signal shaping (LSSS) called approach, the output is not enforced to reach a fixed reference point in a given amount of time,

as long as the shape of the output meets the reference shape. Plants that don't need to comply with strict timing requirements or applications where generating an exact reference is a difficult task by itself, could benefit from this method.

Since LSSS is a just recently introduced concept, [21], the necessary definitions for shape class and harmonic shape class will be discussed in greater detail to provide a better understanding.

3-3-1 Shape Class

Consider a discrete-time signal shape which can be expressed by a linear difference equation, for example an exponentially decreasing function

$$\mathbf{x}(k+1) = \lambda \mathbf{x}(k), \tag{3-30}$$

where $\lambda \in \mathbb{R}$ denotes the exponential decay constant and is restricted to $|\lambda| < 1$. This function can be expressed as

$$\begin{pmatrix} \lambda & -1 \end{pmatrix} \begin{pmatrix} \mathbf{x}(k) \\ \mathbf{x}(k+1) \end{pmatrix} = 0, \tag{3-31}$$

where the vector $\begin{pmatrix} \lambda & -1 \end{pmatrix}$ will be referred to as shape vector.

Equation (3-31) can be used to determine, if any given two consecutive samples of a signal have the properties of a discrete-time signal with the given shape. If the samples indeed exactly meet the shape of this exponential decay, the multiplication of the shape vector with the vector of samples will give zero as result. If on the other hand the two consecutive samples do not meet the shape, e.g. if the samples remain constant, the multiplication will give a value different from zero. Moreover, the more the two consecutive samples conform to the properties of the exponential decay to be investigated, the closer the result will be to zero.

To be able to express this way of comparing signal shapes in a more general way, the shape class is introduced as the set

$$\mathscr{X}_{\mathbf{V}} = \{\mathbf{x}(1), \mathbf{x}(2), \ldots | \mathbf{V} \begin{pmatrix} \mathbf{x}(k+1) \\ \vdots \\ \mathbf{x}(k+T) \end{pmatrix} = \mathbf{0} \; \forall \, k = 0, 1, \ldots\}, \tag{3-32}$$

where $\mathbf{V} \in \mathbb{R}^{s \times nT}$ denotes the shape matrix, n denotes the number of states as previously introduces, T denotes the number of consecutive samples and s denotes the number of states that actually take part in the shape analysis with $s \leq n$. Note that the number of states can differ from the number of states that are compared against a

signal shape. Since this set denotes the elements that are mapped to the zero vector by a linear map, the set (3-32) is also referred to as the kernel of the shape. Goal of the shape analysis is to find the kernel or to determine, if a set is in the neighbourhood of the kernel. If a given set is not part of the kernel, the shape analysis, i.e. the multiplication of the shape matrix with the signal vector, will yield a vector different from the zero vector. This vector different from the zero vector will be referred to as shape residual. To better evaluate how closely a given signal matches a shape, not the shape residual itself is considered, but the distance of the shape residual to the zero vector, i.e. the Euclidean norm

$$\| \mathbf{V}\mathbf{X}(k) \|_2 , \tag{3-33}$$

is used, where $\mathbf{X}(k) = \begin{pmatrix} \mathbf{x}(k+1) & \cdots & \mathbf{x}(k+T) \end{pmatrix}^\intercal$.

To further clarify this concept, consider a signal shape of a step answer of a stable first order system and how it can be determined, if a signal meets the properties of this signal shape. With a discrete-time linear system as

$$x_1(k+1) = 0.8x_1(k) + 0.2x_2(k) \tag{3-34a}$$
$$x_2(k+1) = x_2(k), \tag{3-34b}$$

with the initial states $x_1(0) = 0$, $x_2(0) = 1$, simulating the model for 30 steps result in the discrete-time signals shown in figure 3-1. As can be seen, the evolution of state x_1 resembles the step answer of a first order system, i.e. state x_1 approaches the constant remaining state x_2 in a way, that the next state always will be closer to state x_2 than the current state or will be equal to state x_2. The corresponding shape matrix for

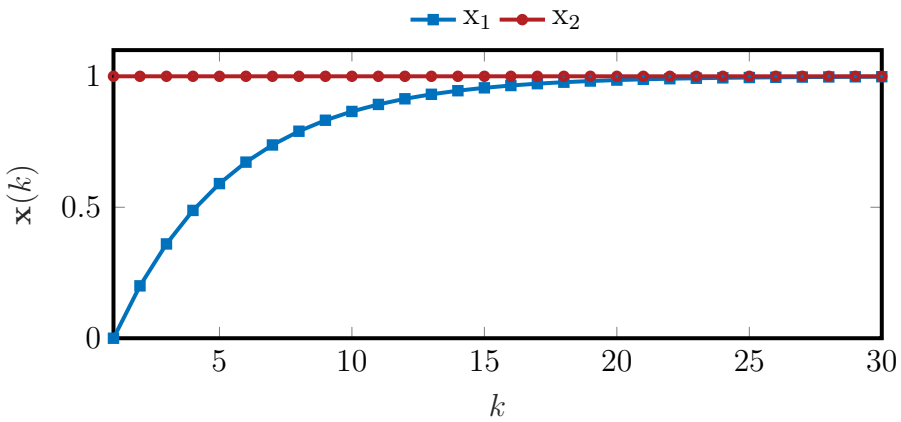

Figure 3-1: Signal evolution of the states of model (3-34).

system (3-34) can be obtained as

$$\mathbf{V} = \begin{pmatrix} 0.8 & 0.2 & -1 & 0 \\ 0 & 1 & 0 & -1 \end{pmatrix}, \tag{3-35}$$

but since only the shape of signal x_1 is of interest, the first row of the shape matrix $\mathbf{V}$ is used so that with $s = 1$, $n = 2$ and $T = 2$ the matrix $\mathbf{V}$ is reduced to $\mathbf{V}_{step} = \begin{pmatrix} 0.8 & 0.2 & -1 & 0 \end{pmatrix}$. To compare the shape of an arbitrary signal x_t against the shape of state x_1, this state is replaced by the signal so that model (3-31) is modified as

$$\hat{x}_1(k+1) = x_t(k) \tag{3-36a}$$
$$\hat{x}_2(k+1) = \hat{x}_2(k), \tag{3-36b}$$

with the initial states $\hat{x}_1(0) = x_t(0)$, $\hat{x}_2(0) = x_2(0) = 1$. The distance of two consecutive state vectors to the zero vector is calculated according to (3-33) by

$$(\mathbf{V}_{step}\hat{\mathbf{x}})^\mathsf{T}\mathbf{V}_{step}\hat{\mathbf{x}}, \tag{3-37}$$

where $\hat{\mathbf{x}} = \begin{pmatrix} x_t(k) & \hat{x}_2(k) & x_t(k+1) & \hat{x}_2(k+1) \end{pmatrix}^\mathsf{T}$.

Figure 3-2 shows the comparison of two different signals x_{t1} and x_{t2} with the given sinal shape. Signal x_{t1} is a linear increasing signal with $x_{t1}(0) = -3$, while x_{t2} follows an exponential decay function in the form of $x_{t2}(k) = 1 - 1.25^{-k}$ which is explicitly modelled to resemble state x_1 of model (3-34) closely. The distance of the shape residual of both signals to the origin is calculated for each $k = 0, \ldots, 9$ according to (3-37) and plotted on a logarithmic scale on the lower part of figure 3-2. As can be seen on the left side of the figure, the distance of two consecutive signals of x_{t1} and thus the dissimilarity to the shape of x_1 increases with increasing k. On the other hand, as signal x_{t2} already is quite similar to x_1, the distance is much lower compared to the distance of x_{t1} and is even decreasing since the approximation of x_1 to an exponential decay function is better the closer x_1 is to x_2.

3-3-2 Harmonic Shape Class

The sinusoidal shape is of particular interest for this thesis. The property of a sine wave can be described by a homogeneous second order ordinary differential equation (ODE)

$$\frac{\mathrm{d}^2 x(t)}{\mathrm{d}t^2} + \omega^2 x(t) = 0, \tag{3-38}$$

where ω denotes the angular frequency of the signal. Solving the initial value problem of this ODE with $x(0) = 0$ and $\frac{\mathrm{d}^2 x(0)}{\mathrm{d}t^2} = 0$ leads to $x(t) = c_1 \sin(\omega t)$ with an arbitrary

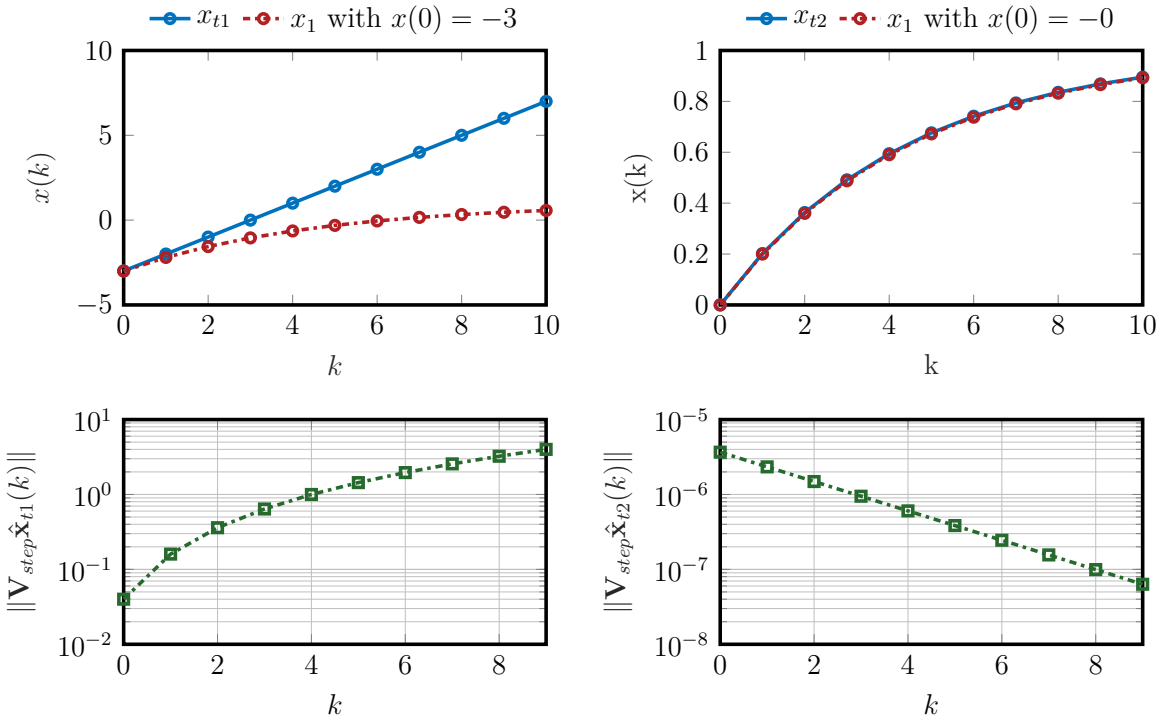

Figure 3-2: Comparison of signals x_{t1} and x_{t2} with x_1. The upper plots show the signal evolution with increasing steps, the lower plots show the distances of the shape residual of two consecutive states of model (3-36) to the shape kernel.

amplitude c_1. In order to fit this property into the form of the shape class (3-32), an approximation of the second derivative using forward numerical differentiation is used, such that

$$\ddot{x}(t) \approx \frac{1}{h^2}\left(2f(x) - 5f(x+h) + 4f(x+2h) - f(x+3h)\right), \tag{3-39}$$

with the step size h. The choice of using four coefficients gives an order of accuracy of $O(h^2)$, [39]. The discrete-time version of (3-39) is

$$\ddot{x}(k) \approx \frac{1}{T_s^2}\left(2x(k) - 5x(k+1) + 4x(k+2) - fx(k+3)\right), \tag{3-40}$$

connecting the approximation step size with the sampling interval T_s. With this approximation, the discrete-time version of the ODE (3-38) can be formulated as

$$\frac{1}{T_s^2}\Big((2+\omega^2 T_s^2)x(k) - 5x(k+1) + 4x(k+2) - x(k+3)\Big) = 0, \tag{3-41}$$

and the shape matrix $\mathbf{V}$ can be obtained as

$$\mathbf{V} = \begin{pmatrix} 2 + (\omega^2 T_s^2) & -5 & 4 & -1 \end{pmatrix}. \tag{3-42}$$

With this shape matrix with $T = 4$ and the resulting shape residual it is possible to determine, if a discrete-time signal resembles the shape of a sinusoidal signal or how much a given signal resembles the shape of sine wave, [21].

3-4 State Shaping by Model Predictive Control

As outlined in the previous section, shape classes provide the possibility to test if a state coincides with a given signal shape. Furthermore shape classes can be used to find a future state sequence with given shape properties by means of an optimization problem similar to that introduced in section 3-2.

It is possible to find an input to any discrete-time linear time invariant system, such that the shape residual of future states when compared against a given shape class will decrease with every step or remain the zero vector. This can be achieved by formulating the optimization problem

$$\min_{\mathbf{X}(k)} \left(\mathbf{V}\mathbf{X}(k)\right)^2. \tag{3-43}$$

Using the prediction (3-11) with a prediction and input horizon $H_p = H_u = T$, the optimization problem transforms into

$$\min_{\Delta\mathcal{U}} \left(\mathbf{V}\mathcal{X}(k)\right)^2 = \min_{\Delta\mathcal{U}} \left(\mathbf{V}\left(\mathbf{\Psi}\mathbf{x}(k) + \mathbf{\Upsilon}\mathbf{u}(k-1) + \mathbf{\Theta}\Delta\mathcal{U}\right)\right)^2. \tag{3-44}$$

Remember that for harmonic shape classes $T = 4$ which would restrict the prediction horizon to $H_p = T = 4$ with this formulation. It is possible to extend the optimization to longer prediction horizons, but to match the dimension and structure of $\mathcal{X}(k)$, the shape matrix has to be transformed into a band matrix. For this let the shape matrix be sliced into parts

$$\mathbf{V}_j = \mathbf{V} \begin{pmatrix} \mathbf{0}^{n(j-1)\times n} \\ \mathbf{I}^{n\times n} \\ \mathbf{0}^{n(T-j)\times n} \end{pmatrix} \text{ for } j = 1, 2, \ldots, T, \tag{3-45}$$

where each $\mathbf{V}_j \in \mathbb{R}^{s\times n}$, so that

$$\mathbf{P}_V = \begin{pmatrix} \mathbf{V}_1 & \mathbf{V}_2 & \cdots & \mathbf{V}_T & \mathbf{0} & \cdots & \mathbf{0} \\ \mathbf{0} & \mathbf{V}_1 & \mathbf{V}_2 & \cdots & \mathbf{V}_T & \ddots & \vdots \\ \vdots & \ddots & \ddots & \ddots & \ddots & \ddots & \mathbf{0} \\ \mathbf{0} & \cdots & \mathbf{0} & \mathbf{V}_1 & \mathbf{V}_2 & \cdots & \mathbf{V}_T \end{pmatrix}, \tag{3-46}$$

with $\mathbf{P}_V \in \mathbb{R}^{p_1 \times p_2}$, where $p_1 = s(H_p - T + 1)$ and $p_2 = nH_p$. As will be shown, this not only enables the formulation of an MPC scheme for linear state signal shaping, but the resulting formulation also matches the regular formulations so well, that standard solving methods can be applied for LSSS MPC.

3-4-1 Formulation of the Unconstrained Optimization Problem

With the definition of $\mathbf{P}_V$ as in (3-46), the minimization problem (3-44) for an arbitrary prediction horizon can be formulated as

$$\min_{\Delta\mathcal{U}} \left(\mathbf{V}\mathcal{X}(k)\right)^2 = \min_{\Delta\mathcal{U}} \left(\mathcal{X}(k)^\intercal \mathbf{P}_V^\intercal \mathbf{P}_V \mathcal{X}(k)\right), \tag{3-47}$$

and with $\mathbf{Q}_S = \mathbf{P}_V^\intercal \mathbf{P}_V$ and a weighting matrix $\mathbf{R}$ as defined in (3-20), the cost function for the LSSS MPC is introduced as

$$J(\Delta\mathcal{U}) = \mathcal{X}(k)^\intercal \mathbf{Q}_S \mathcal{X}(k) + \Delta\mathcal{U}^\intercal \mathbf{R} \Delta\mathcal{U}. \tag{3-48}$$

This cost function closely resembles the cost function of the MPC condense formulation (3-27) with the only difference, that the state weighting matrix $\mathbf{Q}_S$ is not a block diagonal matrix but has the structure of a band matrix since it is derived from the shape matrix. With this difference, the regulator control scheme is transformed into a shape control scheme: instead of driving the states towards an equilibrium, i.e. towards the state zero vector which is the origin, the states are driven towards a minimal shape residual, i.e. the closest possible resemblance to the given shape class. Note that the origin is part of the shape kernel. If it is desired to find an optimal input vector, that leads to a state evolution with a minimal shape residual but without leading the states towards the origin, a proper weighting of the state cost weighting matrix $\mathbf{Q}_S$ and the input cost weighting matrix $\mathbf{R}$ has to be chosen.

The unconstrained LSSS MPC optimization problem can be formulated as a condensed unconstrained MPC problem as shown in equation (3-49) using the state cost weighting matrix $\mathbf{Q}_S$ instead of the regular state cost weighting matrix $\mathbf{Q}$. For the purpose of compensating disturbances, the prediction is extended to also include measured disturbances as shown in equation (3-6). This leads to the unconstrained LSSS MPC problem developed in [21] as

$$\min_{\mathbf{\Delta}\mathcal{U}} \quad \frac{1}{2}\Delta\mathcal{U}(k)\mathbf{P}\Delta\mathcal{U}(k) + \mathbf{q}^\intercal \Delta\mathcal{U}(k), \tag{3-49a}$$

with

$$\mathbf{P} = \mathbf{\Theta}^\intercal \mathbf{Q}_S \mathbf{\Theta} + \mathbf{R}, \tag{3-50}$$

$$\mathbf{q} = -2\mathbf{\Theta}^\intercal \mathbf{Q}_S (\mathbf{\Psi}\mathbf{x}(k) + \mathbf{\Upsilon}\mathbf{u}(k-1) + \mathbf{\Gamma}\mathbf{d}_m). \tag{3-51}$$

For further usage, the state error prediction $\mathcal{E}(k)$ will be defined as

$$\mathcal{E}(k) = \mathbf{\Psi}\mathbf{x}(k) + \mathbf{\Upsilon}\mathbf{u}(k-1) + \mathbf{\Gamma}\mathbf{d}_m. \tag{3-52}$$

As it is the case with any unconstrained QP, the analytical solution of this optimzation problem can be obtained by finding the minimum with

$$\frac{\partial J}{\partial \Delta\mathcal{U}(k)} = 2\Delta\mathcal{U}(k)\mathbf{P} + \mathbf{q}^\intercal \stackrel{!}{=} 0, \tag{3-53}$$

which leads to the solution

$$\Delta\mathcal{U}(k) = \frac{1}{2}\,\mathbf{P}^{-1}(-\mathbf{q})\,, \tag{3-54}$$

since the Hessian is positive semidefinite and thus $\frac{\partial^2 J}{\partial \Delta\mathcal{U}(k)^2} > 0$, which leads to a minimum. Using the square-root formulation as shown in equations (3-28) and (3-29), the optimal input vector can be obtained with

$$\Delta\mathcal{U}(k) = \left[\begin{pmatrix}\mathbf{S}_Q\mathbf{\Theta}\\ \mathbf{S}_R\end{pmatrix}^\intercal \begin{pmatrix}\mathbf{S}_Q\mathbf{\Theta}\\ \mathbf{S}_R\end{pmatrix}\right]^{-1} \begin{pmatrix}\mathbf{S}_Q\mathbf{\Theta}\\ \mathbf{S}_R\end{pmatrix}^\intercal \begin{pmatrix}\mathbf{S}_Q\left(\mathbf{\Psi}\mathbf{x}(k) + \mathbf{\Upsilon}\mathbf{u}(k-1) + \mathbf{\Gamma}\mathbf{d}_m\right)\\ \mathbf{0}\end{pmatrix}, \tag{3-55}$$

which using the Moore-Penrose pseudoinverse can be written as

$$\Delta\mathcal{U}(k) = \begin{pmatrix}\mathbf{S}_Q\mathbf{\Theta}\\ \mathbf{S}_R\end{pmatrix}^\dagger \begin{pmatrix}\mathbf{S}_Q\,\mathcal{E}(k)\\ \mathbf{0}\end{pmatrix}, \tag{3-56}$$

also using the state error prediction as defined in (3-52).

For application, equation (3-56) can be solved by using MATLABs backslash operator. Since only the state error prediction $\mathcal{E}(k)$ changes in every calculation step, the unconstrained LSSS MPC can be seen as a state-feedback controller with the control law

$$\Delta\mathcal{U}(k) = \mathbf{K}_{MPC}\,\mathcal{E}(k), \tag{3-57}$$

where

$$\mathbf{K}_{MPC} = \begin{pmatrix}\mathbf{S}_Q\mathbf{\Theta}\\ \mathbf{S}_R\end{pmatrix}^\dagger \begin{pmatrix}\mathbf{S}_Q\\ \mathbf{0}\end{pmatrix}. \tag{3-58}$$

With z defined as any complex number used for the Z-transformation $\mathscr{Z}\{x(k)\}$, [40], figure 3-3 shows the block diagram of the controller which takes into account the current state $\mathbf{x}(k)$, the last control input $\mathbf{u}(k-1)$ obtained with the unit cycle delay $z^{-1}\,\mathbf{I}$ and the disturbance measurement $\mathbf{d}_m$ to obtain the state error prediction. The control input change $\Delta\mathcal{U}(k)$ is calculated with (3-57) and is passed through a discrete-time integrator $\frac{z}{z-1}\,\mathbf{I}$ to obtain the control input itself.

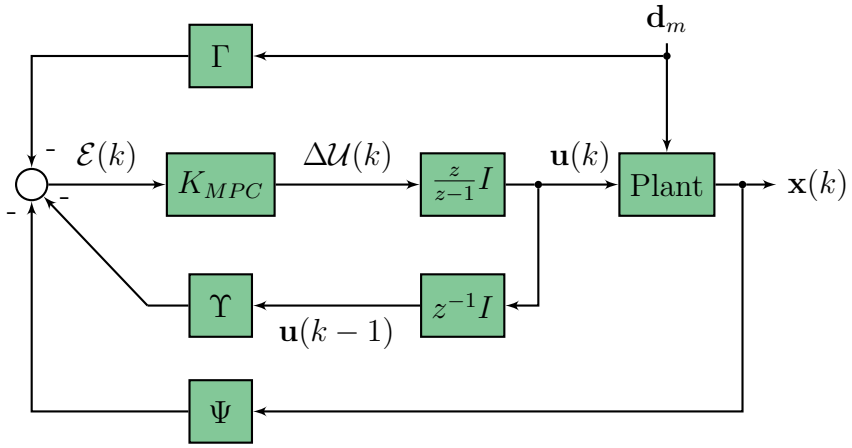

Figure 3-3: Block diagram showing the unconstrained LSSS MPC controller as a state-feedback controller.

3-4-2 Periodic Receding Horizon Strategy

While the RHC approach is commonly applied in MPC as outlined in section 3-2, the LSSS MPC modifies this strategy to a periodic RHC. With this strategy, instead of applying only the first input, the whole calculated optimal input vector is used as input to the plant. As could be shown in [21], this strategy leads to sinusoidal state signals and also has the benefit of only calculating the optimal input vector once every period instead of once every sample step. Using the periodic RHC ties the input horizon H_u to the sampling interval T_s as $H_u = \frac{1}{fT_s}$ with the frequency $f = \frac{\omega}{2\pi}$, which matches the minimum number of steps per period for a given sampling interval. This furthermore means, that the prediction horizon H_p is also tied to the sampling interval, since the input horizon cannot be be larger than the prediction horizon. With this restriction, choosing small sampling intervals to obtain a better discretization can lead to quite large prediction horizons, which could affect the computing time of constrained MPC optimization problems.

3-4-3 Assumptions and Limitations

For problem (3-47) the following assumptions are made:

Assumption 1. Strong convexity is assumed to obtain a minimum at all times. This assumption relies on the property of the Hessian, which is assumed to be positive semi-definite.

Assumption 2. When applying the periodic RHC strategy, it is assumed that the measured disturbances for the next period is the same as the measured disturbance for the current period.

Assumption 3. Full state measurement without delay is available for the targeted states by the controller.

As could be shown in [21], while an optimal control input sequence can be found to bring a targeted state into a sinusoidal shape, the amplitude magnitude of the signal can increase or decrease depending on the tuning of the weighting matrices $\mathbf{R}$ and $\mathbf{Q}_S$. Since at the time of writing this thesis the only tuning strategy for the developed control method relies on heuristic parameter variation, the LSSS MPC does not lead to a reliable steady state behaviour with different measured disturbances. Moreover, with the concept it is not possible to bring the signal to a predefined amplitude.

Chapter 4

Linear State Signal Shaping MPC Amplitude Control

This chapter introduces methods developed in the scope of the thesis to solve the problems outlined in section 3-4-3. Section 4-1 portrays numerical properties of the unconstrained linear state signal shaping (LSSS) model predictive control (MPC). For verification of the solution approach presented, a model based on the grid representation shown in figure 2-5 is developed. Section 4-3 forms the core part of this chapter, providing methods on how different kinds of constraints can be applied to the LSSS MPC method, accompanied by simulation results using the previously introduced state space model.

4-1 Numerical properties of the Unconstrained Linear Signal Shaping MPC

The harmonic shape class as introduced in section 3-3-2 employs a forward numerical differentiation in order to approximate the second derivative of an arbitrary signal. In order to assess the numerical properties of this approximation, the analysis of the unconstrained LSSS MPC as conducted in the work which first introduced this control method, is extended by an approximation error estimation.

4-1-1 Harmonic Shape Class Approximation Error

Given a row vector of approximation coefficients $\boldsymbol{\alpha} \in \mathbb{R}^{1\times a}$ as derived in [39], where a corresponds to the number of coefficients, the approximation error for numerical differentiation is evaluated by computing the Euclidean norm

$$\left\|\ddot{\mathbf{x}}(k) - \hat{\ddot{\mathbf{x}}}(k)\right\| = \sqrt{\sum_{k} \left|\ddot{x}(k) - \hat{\ddot{x}}(k)\right|^2}, \tag{4-1}$$

where $\ddot{x}(k) = -\omega^2 \sin(\omega k)$ denotes the second time derivative of a discrete-time normalized sine wave $x(k) = \sin(\omega k)$ and $\hat{\ddot{x}}(k) = \frac{\boldsymbol{\alpha}}{T_s^2}\begin{pmatrix} x(k) & x(k+1) & \cdots & x(k+a)\end{pmatrix}^\intercal$ according to (3-41) denotes the approximation of the second derivative by means of forward numerical differentiation. For central numerical differentiation the approximation error is calculated accordingly, but here the approximation of the second derivative is shifted, so that $\hat{\ddot{x}}(k) = \boldsymbol{\alpha}\begin{pmatrix} x(k-\frac{(a-1)}{2}) & x(k-\frac{(a-1)}{2}+1) & \cdots & x_{d0}(k-\frac{(a-1)}{2}+a)\end{pmatrix}^\intercal$. Note that only odd numbers of coefficients exist for central approximations.

Figure 4-1 depicts the result of the approximation error analysis, comparing both central and forward numerical differentiation with an increasing number of coefficients. A sampling interval of $T_s = 0.2\,\text{ms}$ for the discrete-time sine wave signal is chosen, the approximation is conducted for one period. As can be seen, the approximation error decreases with an increasing number of coefficients. Also the central approximation yields a lower approximation error with the same number of coefficients as compared

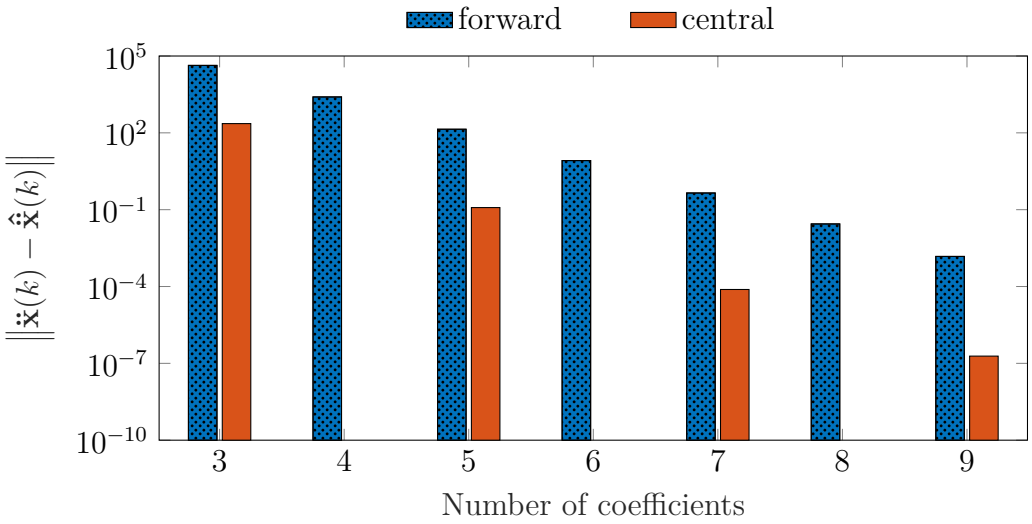

Figure 4-1: Comparison of errors between forward and central numerical differentiation to approximate the second derivative of a sine wave.

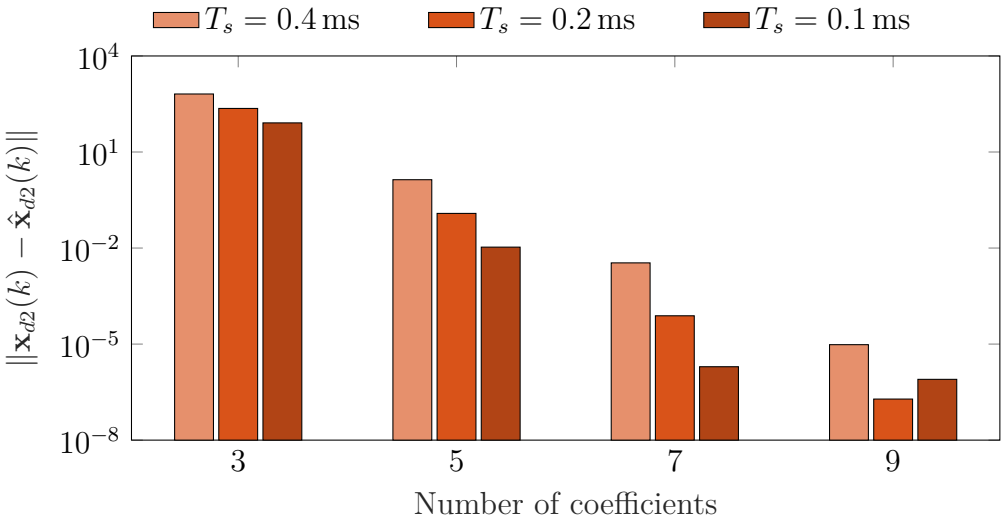

Figure 4-2: Central approximation error with different sampling times T_s.

to the forward numerical differentiation. The error also decreases with smaller sampling intervals as shown in figure 4-2, which is expected, since interpolation points are spaced more closely, resulting in a more accurate approximation, [41]. Interestingly, the approximation error with nine coefficients is lower for a sampling time of $T_s = 0.2\,\text{ms}$ than the error with $T_s = 0.1\,\text{ms}$, which could be due to a computing precision error, since $\frac{\alpha}{T_s^2}$ yields higher values with decreasing sampling intervals.

4-1-2 Hessian Condition Number

An important metric for numeric solvers that use any kind of gradient descent method, is the condition number of the Hessian due to the relation between complexity bounds for solving a problem and the condition number of the problem, [42]. Given a matrix $\mathbf{M}$, the condition number is defined as

$$\kappa(\mathbf{M}) = \frac{|\lambda_{max}(\mathbf{M})|}{|\lambda_{min}(\mathbf{M})|}, \tag{4-2}$$

where $\lambda_{max}(\mathbf{M})$ denotes the maximum eigenvalue of $\mathbf{M}$ and $\lambda_{min}(\mathbf{M})$ denotes its minimum eigenvalue. For singular matrices, gradient descent algorithms do not converge and the condition number is infinite. The higher the condition number, the closer the matrix is to singularity and hence the more ill-conditioned it is.

Condition numbers for the Hessian (3-50) of the unconstrained LSSS MPC problem are calculated according to equation (4-2), where the state cost weighting matrix $\mathbf{Q}_S$ is

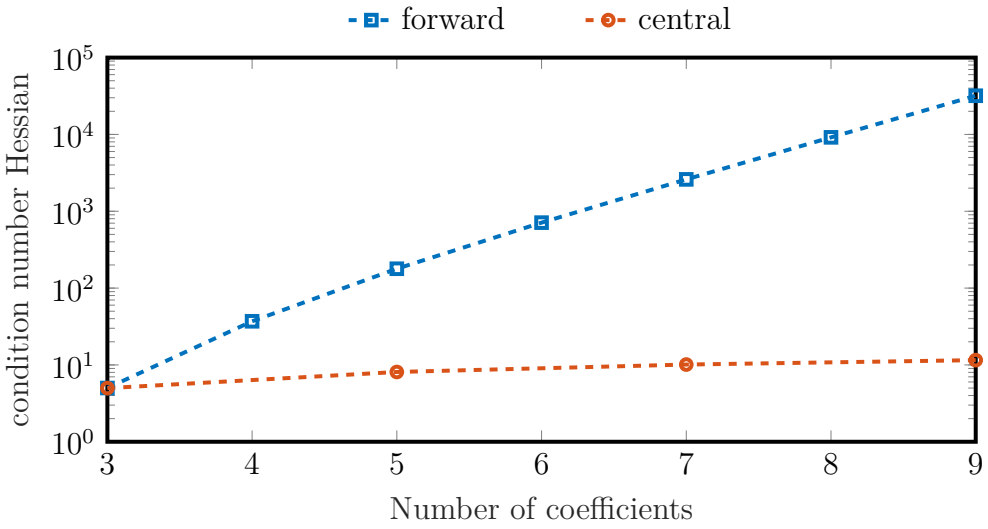

Figure 4-3: Comparison of condition numbers for forward and central numerical approximation.

calculated with different numbers of coefficients both for central and forward numerical differentiation to approximate the harmonic shape class. As input cost weighting matrix $\mathbf{R}$ the identity matrix is chosen. Figure 4-3 shows the results of this comparison. With an increasing number of coefficients, the Hessian gets more ill-conditioned, while the ill-conditioning advances faster when using forward approximation.

As a conclusion to the numerical properties of the unconstrained LSSS MPC, using central numerical differentiation shows advantages compared to using forward numerical differentiation, which is used in previous publications, [21, 43, 22]. Also smaller numbers of coefficients are preferred when a numerical solver is needed to solve the optimization problem, as this is the case when constraints are applied.

4-2 Single Phase System Model

As outlined in section 2-1, shunt active power filters (SAPF) are used to compensate current harmonics, which are typically drawn from the grid by nonlinear loads. Voltage source converters (VSC) are used to inject the compensation current into the grid. The output of the VSC depends on the control signals driving the power electronic switches. The combination of the grid with the SAPF can be seen as hybrid dynamic system, since both time continuous grid dynamics as well as event discrete switching dynamics are present. Although methods exist to model this hybrid dynamic system, [44], in

order to reduce modelling complexity an equivalent circuit as shown in figure 4-4 is used to describe the system dynamics. With this system model, the control goal is to compensate the current i_l with the current i_{c0} in such a way, that the feeder line current i_f is sinusoidal.

4-2-1 Equivalent Circuit

Figure 4-4 shows the equivalent circuit for one phase of the grid connected SAPF and a nonlinear load. The controlled voltage source v_s provides alternating voltage, R_1 and L_1 represent the transmission resistance and inductance respectively to model the transmission feeder line with the current i_f. Instead of an event based switching VSC, a non-ideal current source consisting of a controllable ideal current source i_{c0} and internal resistance R_3 is used. To induce the compensating current into the grid, a coupling resistance R_2 and a coupling inductance L_2 are used, also acting as a smoothing filter. The filtered current i_c is injected at the point of common coupling (PCC). The harmonic current i_l drawn by the nonlinear load is modelled as an ideal current source i_{l0} with the internal resistance R_4.

In this model, v_s and i_l act as measured disturbances to the system and the controller is supposed to find the optimal compensation current i_{c0} to bring the feeder line current i_f to a sinusoidal shape.

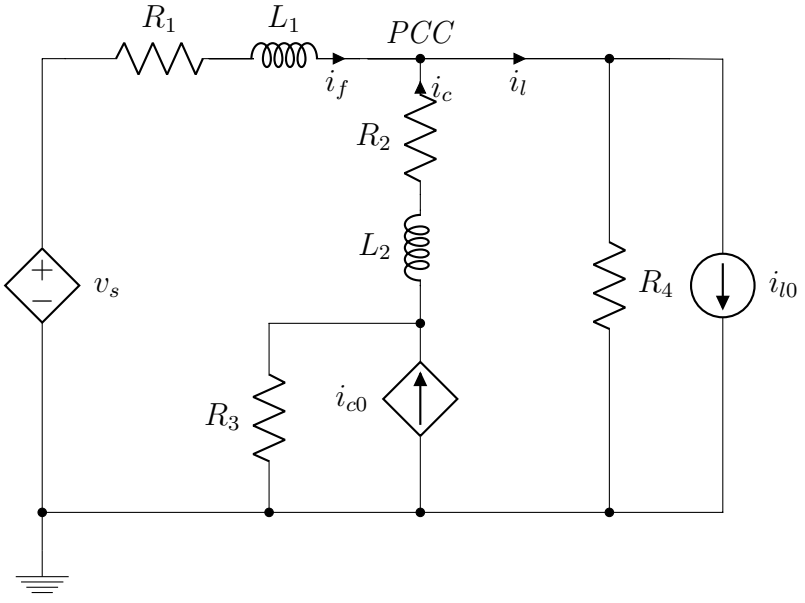

Figure 4-4: Equivalent circuit of the grid using ideal current sources.

Table 4-1: Parameters for the equivalent circuit shown in figure 4-4.

Transmission		Compensation Coupling		Internal Resistances	
R_1	L_1	R_2	L_2	R_3	R_4
$1\,\Omega$	$10\,\mu\mathrm{H}$	$0.05\,\Omega$	$3.5\,\mathrm{mH}$	$10\,\mathrm{k}\Omega$	$10\,\mathrm{k}\Omega$

Using Kirchhoff's current and voltage laws, a set of differential equations can be developed to model the dynamics of the equivalent circuit shown in figure 4-4 with

$$-v_s + R_1 i_f + L_1 \frac{\mathrm{d}i_f}{\mathrm{d}t} - R_2 i_c - L_2 \frac{\mathrm{d}i_c}{\mathrm{d}t} + R_3 \left(i_{c0} - i_c\right) = 0\,, \tag{4-3}$$

$$-R_3 \left(i_{c0} - i_c\right) + R_2 i_c + L_2 \frac{\mathrm{d}i_c}{\mathrm{d}t} + R_4 \left(i_l - i_{l0}\right) = 0\,, \tag{4-4}$$

$$i_f + i_c = i_l\,. \tag{4-5}$$

Reordering these equations and replacing i_l in (4-4) with (4-5) leads to a linear time-invariant system of differential equations

$$\begin{pmatrix} \frac{\mathrm{d}i_f}{\mathrm{d}t} \\ \frac{\mathrm{d}i_c}{\mathrm{d}t} \end{pmatrix} = \begin{pmatrix} -\frac{R_1+R_4}{L_1} & -\frac{R_4}{L_1} \\ -\frac{R_4}{L_2} & -\frac{R_2+R_3+R_4}{L_2} \end{pmatrix} \mathbf{x}(t) + \begin{pmatrix} 0 \\ \frac{R_3}{L_2} \end{pmatrix} u(t) + \begin{pmatrix} \frac{1}{L_1} & \frac{R_4}{L_1} \\ 0 & \frac{R_4}{L_2} \end{pmatrix} \mathbf{d}_m(t)\,, \tag{4-6}$$

with the state vector $\mathbf{x}(t) = \begin{pmatrix} i_f & i_c \end{pmatrix}^\mathsf{T}$, the input $u(t) = i_{c0}$ and the vector of measured disturbances $\mathbf{d}_m(t) = \begin{pmatrix} v_s & i_{l0} \end{pmatrix}^\mathsf{T}$. Since the LSSS MPC uses a discrete-time state space representation, this continuous-time model is discretized using zero-order hold with a fixed sampling time T_s to obtain a model as introduced in (3-6), [40]. Table 4-1 shows the model parameters used for simulations of this systems.

4-2-2 Measured Disturbance

When comparing different simulation runs, the periodic disturbance signal

$$i_{l0} = 10\sin(\omega_f t) + 5\sin(5\,\omega_f t) + 3\sin(7\,\omega_f t)\,, \tag{4-7}$$

with a fundamental angular frequency of $\omega_f = 100\pi\ \mathrm{rad\,s^{-1}}$ as shown in figure 4-5 is used as the current drawn by a nonlinear load. The left plot shows the signal in time domain, while the plot on the right shows the frequency domain spectrum. The disturbance signal consists of a fundamental frequency of 50 Hz along with the 5th and 7th harmonic. This artificial disturbance signal is chosen to resemble the harmonic spectrum of a rectifier, which is a typical nonlinear load often found in power electronic

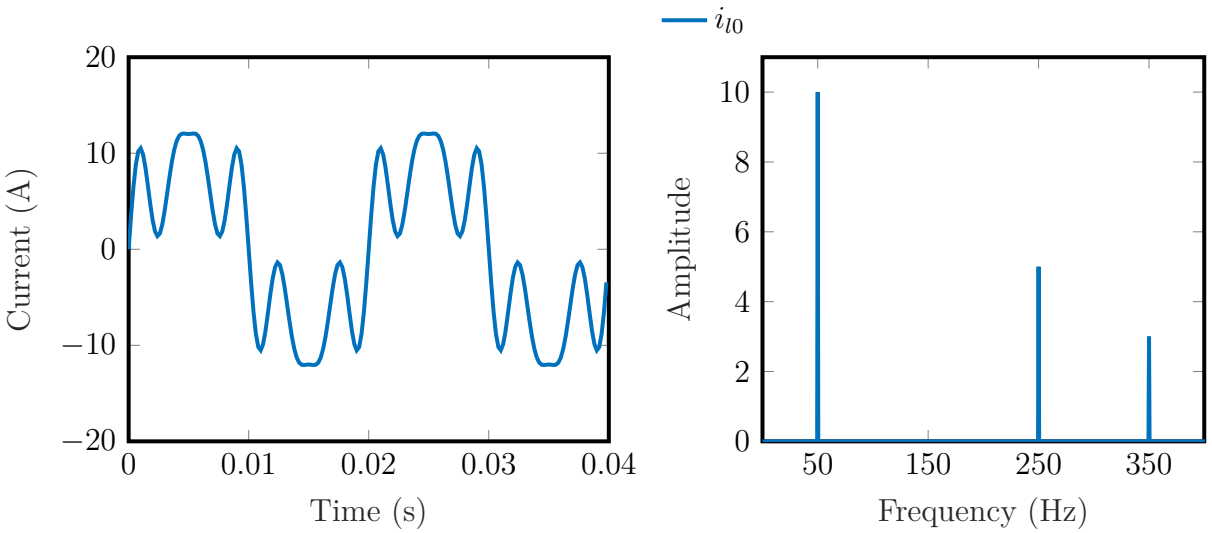

Figure 4-5: Disturbance signal i_{l0} in time domain and frequency domain.

applications. The total harmonic distortion (THD) of this disturbance signal as defined in equation (2-2) is 58.3 %. The second measured disturbance signal v_s is a sine wave with an amplitude of $230\sqrt{2}$ V and a frequency of 50 Hz, which corresponds to the mains power single phase utility voltage in Germany.

4-2-3 Simulation Setup

The main focus of this thesis is to extend the LSSS MPC with constraints, hence a numerical solver is needed to calculate the optimal input. For this purpose the OSQP solver is used, [45]. The convergence tolerance is set to $\varepsilon = 10^{-8}$, which defines the stop criterion for the solver. All simulations are computed using MATLAB R2017b exclusively. Average computing times are determined by running the solver for an optimization problem for $N = 100$ times and calculating the mean of the run time for each solution. Numerical tests are executed on an Intel®Pentium®CPU G3260 @ 3.3 GHz, running Microsoft®Windows 7™.

Regardless of the method used, every simulation is set up in the following manner if not explicitly denoted otherwise:

1. Discretize the system model (4-6) using zero-order hold with a fixed sampling time as denoted.
2. Build up prediction matrices Ψ, Υ, $\boldsymbol{\Theta}$ and Γ using the parameters of the discretized state space model and build up $\mathbf{Q}_S$ and $\mathbf{R}$ as outlined in section 3-4.

3. Simulate the discrete-time model with the signal of the measured disturbances and with a control input of zero for one period to obtain the initial state for the first optimal input calculation.

4. Initialize the solver with the Hessian $\mathbf{P}$ and the linear objective $\mathbf{q}$ as well as constraints.

5. Calculate the optimal input vector and use the whole input vector if using periodic receding horizon control (RHC) or only the first input if using conventional RHC respectively.

6. Simulate the discrete-time model with the new input and the given initial state and store the last state vector as initial state for the next solving step.

7. Update the problem data for the solver with the new initial state and if using the condensed problem formulation also with the last calculated input.

8. Repeat from step five until the simulation is aborted or the maximum simulation time is reached.

For all simulations only diagonal uniformly weighted input weighting matrices are used, hence for simplification the notation

$$\mathbf{R} = \rho \mathbf{I}^{H_u}, \tag{4-8}$$

is used, with ρ denoting the input weighting factor. The MATLAB code for the simulations shown in this chapter can be found on the CD accompanying this thesis.

4-3 Linear State Signal Shaping MPC as a Quadratic Programming Problem

One of the problems of the current LSSS MPC approach is the inability to fix the amplitude of the targeted sinusoidal state. Since the MPC control method inherently is able to include constraints into the optimization problem, this section shows how to extend the LSSS MPC with state constraints.

4-3-1 Linear Constraints with Condensed Problem Formulation

Analogously to the condensed MPC problem formulation (3-49), state constraints can be incorporated to the LSSS MPC problem (3-47) with

$$\min_{\mathbf{\Delta}\mathcal{U}} \quad \frac{1}{2}\Delta\mathcal{U}(k)\mathbf{P}\Delta\mathcal{U}(k) + \mathbf{q}^\intercal\Delta\mathcal{U}(k) \tag{4-9a}$$

$$\text{subject to} \quad \mathbf{l} \leq \mathbf{\Theta}\Delta\mathcal{U}(k) \leq \mathbf{o}\,, \tag{4-9b}$$

with

$$\mathbf{P} = \mathbf{\Theta}^\intercal\mathbf{Q}_S\mathbf{\Theta} + \mathbf{R}, \tag{4-10}$$

$$\mathbf{q} = -2\mathbf{\Theta}^\intercal\mathbf{Q}_S\,\mathcal{E}(k), \tag{4-11}$$

$$\mathbf{l} = \mathbf{x}_{min} - \mathcal{E}(k), \tag{4-12}$$

$$\mathbf{o} = \mathbf{x}_{max} - \mathcal{E}(k), \tag{4-13}$$

where $\mathbf{x}_{max} \in \mathbb{R}^n$ denotes the maximum state constraint vector containing upper limits for each state and $\mathbf{x}_{min} \in \mathbb{R}^n$ denotes the minimum state constraint vector containing lower limits for each state. The targeted state is the first state i_f, therefore only constraints for this state will be applied and the constraints for the second state i_c will be set to $\pm\inf$. With this formulation it is also possible to compute the unconstrained solution by setting $\mathbf{x}_{max} = \begin{pmatrix}\inf & \inf\end{pmatrix}^\intercal$ and $\mathbf{x}_{min} = \begin{pmatrix}-\inf & -\inf\end{pmatrix}^\intercal$, hence not constraining the solution space at all.

When applying constraints, there does no longer exist a fixed state feedback gain $\mathbf{K}_{MPC}$, but instead a dynamic state feedback gain is applied. Figure 4-6 shows a modified ver-

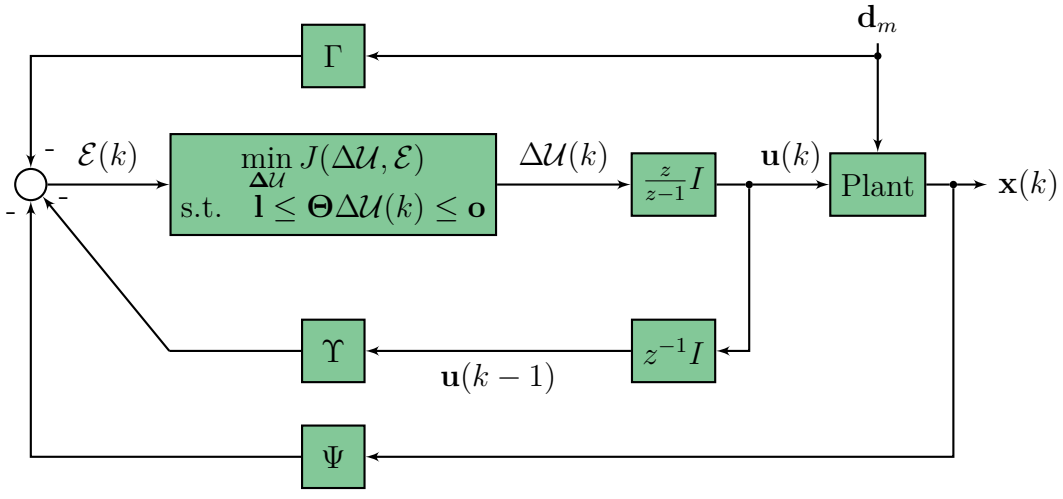

Figure 4-6: Block diagramm of the constrained LSSS MPC controller.

sion of the block diagram in figure 3-3, where the state feedback gain block is exchanged by a dynamic block that symbolizes solving the optimization problem.

Figures for all following simulations contain a parameter annotation box, showing the sampling interval T_s, the prediction horizon H_p, the input horizon H_u, the input weighting factor ρ and which approximation coefficients $\boldsymbol{\alpha}$ are used, where in the notation "$\boldsymbol{\alpha}$: cen3" the number of coefficients is stated and the prefix "cen" denotes central notation while the prefix "for" denotes forward approximation. Applied state constraints are listed as $c\{i_f\} = \pm|i_{f,max}|$ with $i_{f,max}$ denoting the upper current constraint for the feeder line current.

Figure 4-7 shows the simulation results for the LSSS MPC SAPF approach using the OSQP solver and constraints on i_f of $\pm\,\text{inf}$ to obtain the unconstrained solution. In this simulation the periodic RHC strategy is applied. The upper plot shows the feeder line current i_f, the lower plot shows the computed compensation current i_{c0}. After the first period, which is used to store the disturbance signal for one whole period, the controller finds a compensation current to reduce the harmonics of the feeder line current. The THD is reduced from 58.3 % to a value of 0.025 % in the period from $t = 0.12$ s

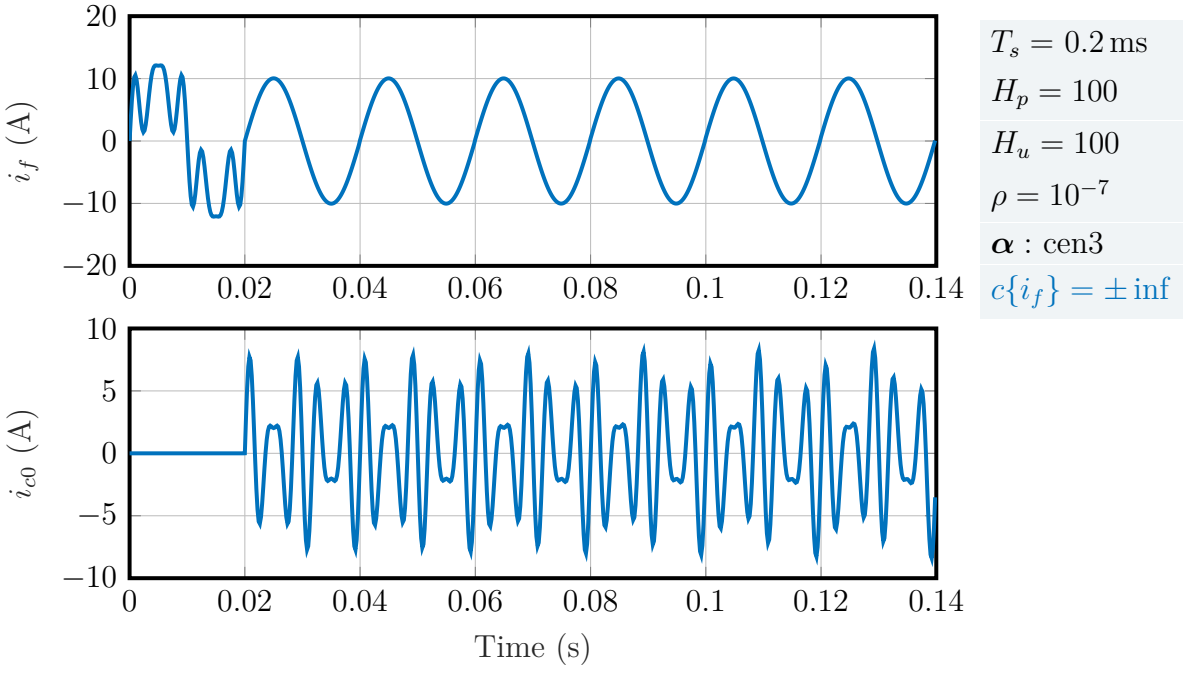

Figure 4-7: Simulation of the system controlled with LSSS MPC using the OSQP solver. No constraints are applied. The upper plot shows the feeder line current, the lower plot shows the compensation current.

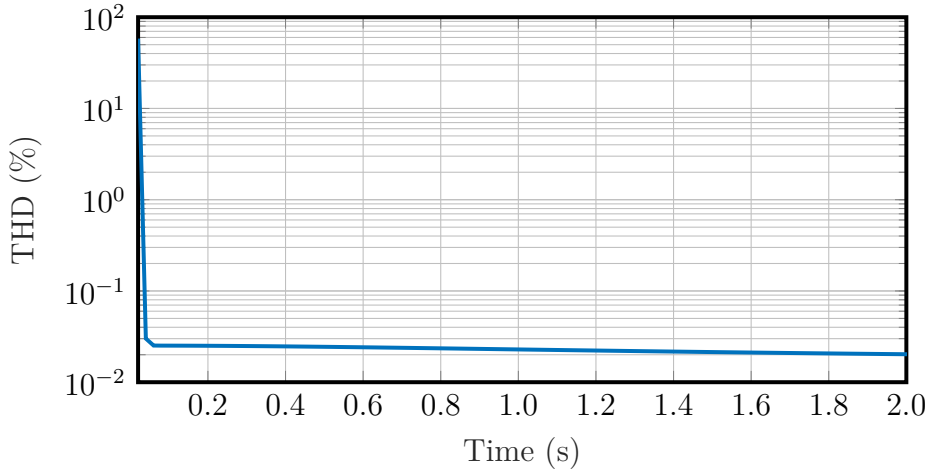

Figure 4-8: THD of the feeder line current when using the period RHC stratety and applying constraints on i_f of $\pm\,\mathrm{inf}$.

to $t = 0.14$ s. The average computing time for solving this optimization problem is 3.13 ms. For small simulation times as shown in figure 4-7, the amplitude of the state signal does not seem to increase, but for longer simulation times the effect of an increasing amplitude magnitude as outlined in section 3-4-3 becomes visible. This effect also is noticeable in figure 4-8, where the evolution of the THD, which is calculated at the beginning of each period, is shown. After an initial dip from 58.3 % to below 0.1 %, the THD slowly but constantly decreases further. This THD decrease happens at the expense of an increasing compensation current, which leads to an increasing amplitude magnitude of the feeder line current. This effect can be prevented by applying state constraints.

Figure 4-9 shows the comparison of simulation runs where different constraints are applied to the feeder line current. As can be seen, the states indeed are limited to the defined constraints of $c\{i_{f2}\} = \pm 8$ and $c\{i_{f3}\} = \pm 4$ and the amplitude magnitude is not increasing after the first period. The average computing time is slightly increased when applying constraints compared to the unconstrained solution with an average computing time of 4.9 ms.

Since state constraints are only capable of defining upper and lower state limits, driving the state to higher amplitude magnitudes than that of the first compensated period merely can be achieved by finding a suitable tuning between the input cost and the state cost. Figure 4-10 shows a simulation where this strategy is applied. A tuning is found, such that the feeder line current constantly rises, if no state constraints are applied. When constraining i_f to ± 13 A, the limits are met. Note that this approach

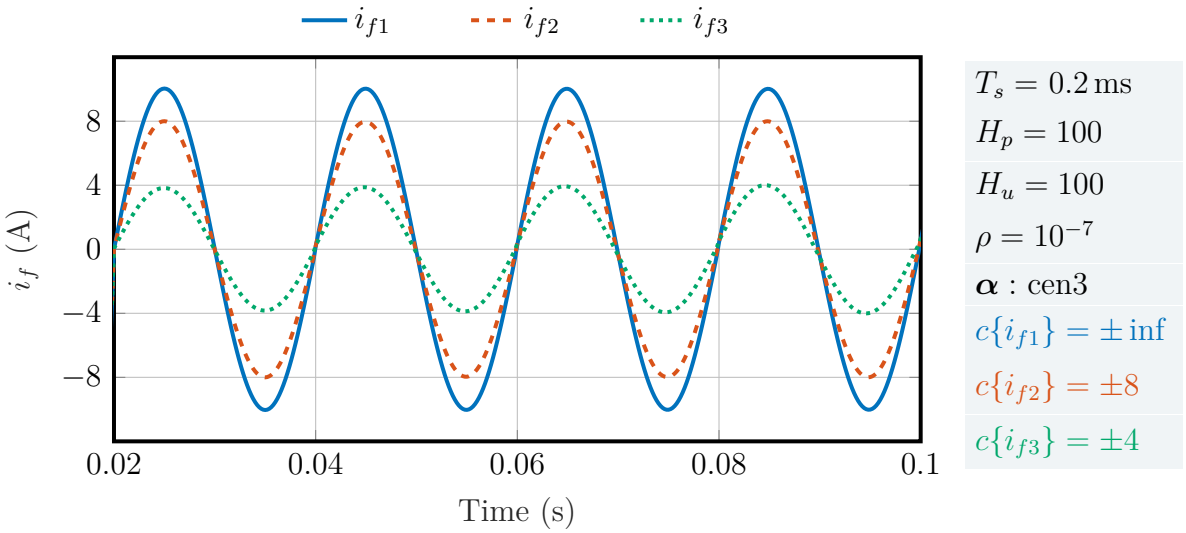

Figure 4-9: Comparison of the compensated feeder line currents with different state constraints applied.

heavily depends on an heuristic tuning of state and input cost weighting factors. Further analysis of the influence of the weighting factors to the solutions is needed to be able to

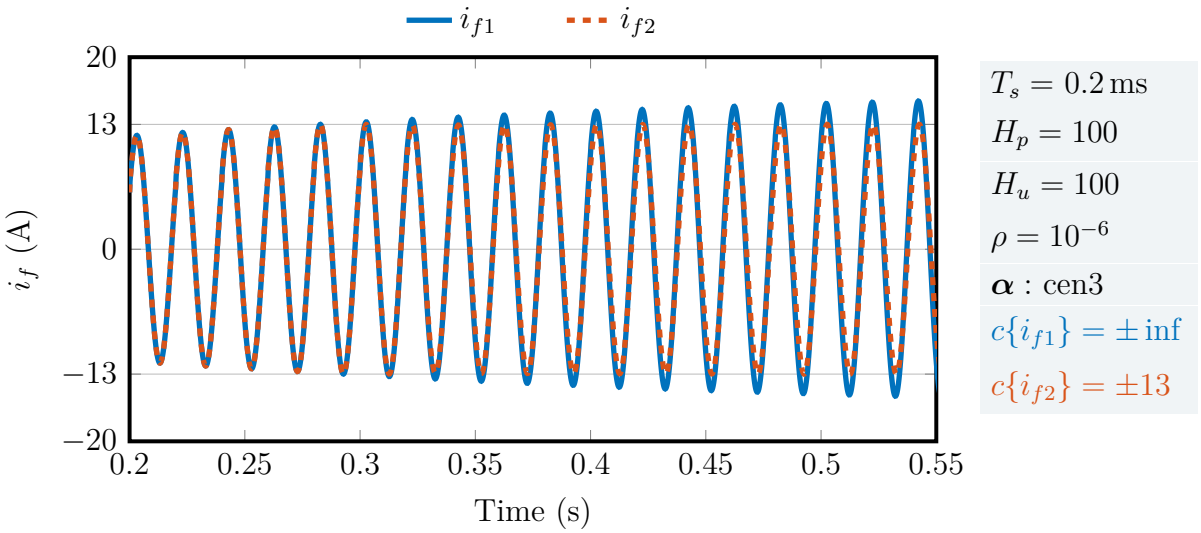

Figure 4-10: Driving the feeder line current to higher amplitude magnitudes by adjusting the tuning between input cost and state cost and then constraining the state.

reliably predict, if the state signal amplitude magnitude will keep increasing. If there do not exist methods to systematically increase the amplitude magnitude to a desired value, it may not be possible to drive the state to an arbitrarily high amplitude.

In order to set the amplitude magnitude to a reference value, the solution space of the optimization problem needs to be restricted in such a way, that solutions leading to sine waves with smaller amplitudes should be excluded. This is not possible with state constraints in general, which only allow to exclude solutions leading to higher amplitude magnitudes. To restrict the solution space in the desired way, the cost function could be enhanced to include the distance of the current state root mean square (RMS) to the desired state RMS. However, since the RMS itself is a quadratic function, calculating the Euclidean norm to obtain the distance would lead to a fourth order cost function. This in turn means, that the optimization problem is transformed from a quadratic program (QP) into a biquadratic program, greatly increasing the complexity and solving time, [33]. Still, if it can be proven, that this optimization problem remains convex, solving this problem in polynomial time is possible in general. Exploiting the structure of the biquadratic problem, which still closely resembles a QP, could even make this approach viable, but this needs further investigation into the numerical properties of this optimization problem.

The analysis of the numerical properties of the unconstrained LSSS MPC in section 4-1 showed, that using higher numbers of coefficients benefits the approximation accuracy. However, when simulating the LSSS MPC SAPF with five approximation coefficients, an increase in THD from 0.03 % to 2.87 % can be observed. This effect arises due to the fact, that with more approximation coefficients more future state predictions are used to build up the state cost weighting matrix $\mathbf{Q}_S$. Hence when the second derivative of the last predicted state $\mathbf{x}(k+H_p)$ is approximated via central numerical approximation with five coefficients, $\mathbf{x}(k+H_p-2), \mathbf{x}(k+H_p-1), \ldots, \mathbf{x}(k+H_p+2)$ are needed, but only $\mathbf{x}(k+H_p-2), \mathbf{x}(k+H_p-1), \ldots, \mathbf{x}(k+H_p)$ are available, yielding an additional approximation error on top of the numerical approximation error. The upper plot in figure 4-11 shows this effect, which leads to a discontinuous feeder line current at the start of each new period due to the amplified approximation error. This effect also appears when using three approximation coefficients, but since only one future state prediction is missing at the end of the prediction horizon for a complete approximation of the second derivative, the error remains small.

The undesired effect due to the amplified approximation error can be cancelled by modifying the periodic RHC strategy in such a way, that a longer prediction horizon $2 \cdot H_p$ is chosen, but only the optimal input vector for one period is used as input for the plant. This way the approximation error still exists at the end of the prediction horizon, but these calculated optimal input values are never used as actual input to the plant. As can be seen in the lower part of figure 4-11, this strategy leads to satisfying results, the THD is reduced to 0.03 %. However, the average computation time is around ten

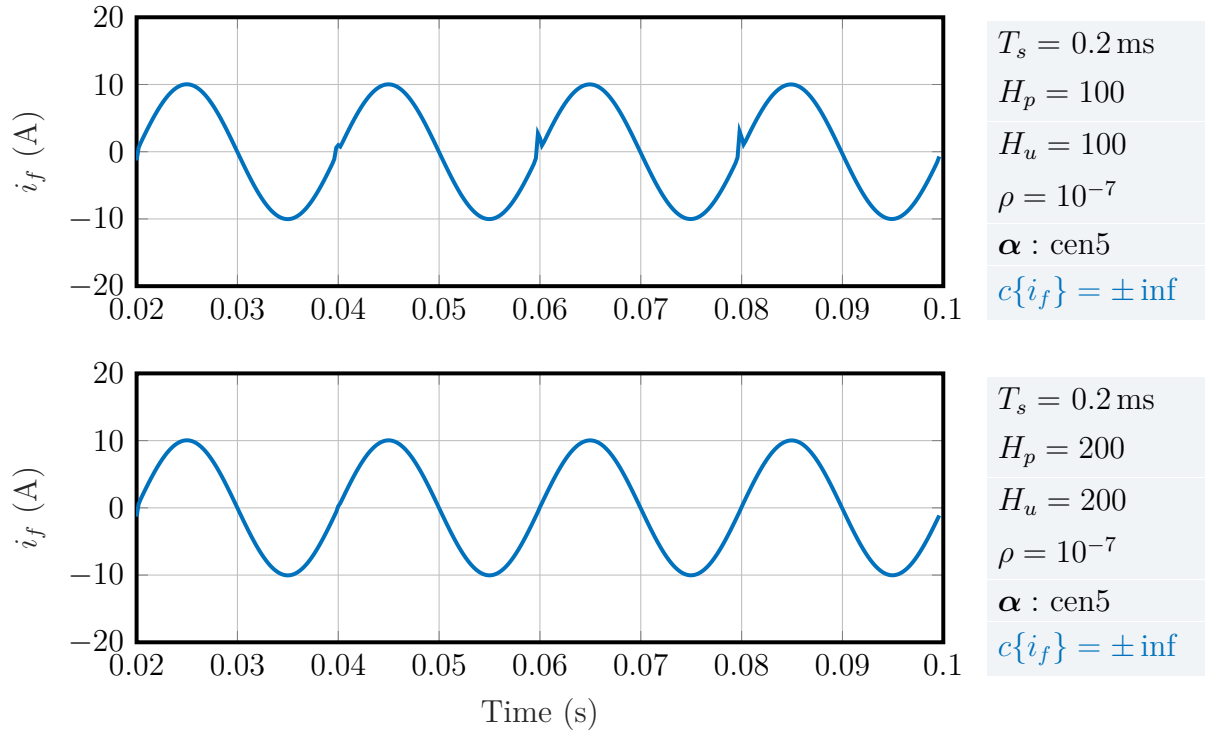

Figure 4-11: Using central numerical approximation with five coefficients leading to an increased THD (upper plot). In the lower plot also five coefficients are used, but the prediction horizon is elongated.

times slower than the computation time of solving this problem with three approximation coefficients without elongated prediction horizon and with no noticeable THD difference.

4-3-2 Linear Constraints with Sparse Problem Formulation

The constrained LSSS MPC optimization problem can be solved using the sparse MPC problem formulation (3-18) by extending the equality constraint with the measured disturbance as

$$\begin{aligned} \min_{\mathbf{z}} \quad & \frac{1}{2}\mathbf{z}^\intercal \mathbf{P}\mathbf{z} && \text{(4-14a)} \\ \text{subject to} \quad & \mathbf{F}\mathbf{z} = \mathbf{c} && \text{(4-14b)} \\ & \underline{\mathbf{z}} \leq \mathbf{z} \leq \overline{\mathbf{z}}, && \text{(4-14c)} \end{aligned}$$

with the Hessian

$$\mathbf{P} = \begin{pmatrix} \mathbf{0}^{n\times n} & \mathbf{0} & \mathbf{0} \\ \mathbf{0} & \mathbf{Q}_S & \mathbf{0} \\ \mathbf{0} & \mathbf{0} & \mathbf{R} \end{pmatrix}, \tag{4-15}$$

appropriate matrices for the equality constraint

$$\mathbf{F} = \begin{pmatrix} \hat{\mathbf{A}} & \hat{\mathbf{B}} \end{pmatrix} \text{ with } \hat{\mathbf{A}} = \begin{pmatrix} -\mathbf{I}^n & \mathbf{0} & \mathbf{0} & \mathbf{0} \\ \mathbf{A} & -\mathbf{I} & \mathbf{0} & \mathbf{0} \\ \mathbf{0} & \mathbf{A} & -\mathbf{I} & \mathbf{0} \\ \mathbf{0} & \mathbf{0} & \mathbf{0} & \ddots \end{pmatrix}, \hat{\mathbf{B}} = \begin{pmatrix} \mathbf{0}^{1\times H_p} \\ \mathbf{I}^{H_p} \end{pmatrix} \otimes \mathbf{B}, \tag{4-16}$$

and vector

$$\mathbf{c} = \begin{pmatrix} -\mathbf{A}\mathbf{x}(k) & -\mathbf{E}\mathbf{d}_m(k-H_p) & -\mathbf{E}\mathbf{d}_m(k-H_p+1) & \cdots & -\mathbf{E}\mathbf{d}_m(k-1) \end{pmatrix}^\intercal, \tag{4-17}$$

where $\begin{pmatrix} \mathbf{d}_m(k-H_p) & \mathbf{d}_m(k-H_p+1) & \cdots & \mathbf{d}_m(k-1) \end{pmatrix}^\intercal$ corresponds to the vector of measured disturbances of the previous period. Simulations show, that similar but not identical solutions are calculated, when finding the optimal input to compensate non-linear feeder line currents. An important difference between formulations is the way the input is weighted in the respective cost functions. While the input is weighted in terms of input differences when using the condensed problem formulation, the sparse formulation directly adds the weighted input as cost to the cost function. This means that the cost weighting factor has a different effect on the solution for each problem formulation.

Table 4-2 shows the simulation results for a comparison between both sparse formulated and condensed formulated LSSS MPC feeder line current compensations with different sampling intervals T_s, using the periodic RHC strategy. Both simulations use three central approximation coefficients to compose the state weighting matrix $\mathbf{Q}_S$, while for each condensed formulation a weighting factor of $\rho = 10^{-7}$ and for each sparse formulation a weighting factor of $\rho = 10^{-8}$ is used. Recalling that the prediction horizon H_p is tied to T_s, it is expected, that using smaller sampling intervals, i.e. better discretization, will yield better compensation results and thus lower THD of the feeder line current i_f. This assumption holds true when using the condensed problem formulation, but not for the sparse problem formulation, where the overall THD of the feeder line current is worst when using the smallest sampling interval of $T_s = 0.1\,\text{ms}$. This effect could be the result of a suboptimal cost weighting factor tuning. Further analysis of the influence of tuning factors on the performance of the sparse problem solver is needed, which is not part of the scope of this thesis.

When comparing the average computing times for solving the optimization problems, the sparse solver outperforms the condensed solver in any setup and is faster roughly

Table 4-2: Comparison of harmonic compensation with both sparse formulated and condensed formulated LSSS MPC optimization problems for different state limits of the feeder line current i_f and different sampling intervals T_s. The lower part of the table shows average solving times for both problems.

	THD with $T_s = 0.4\,\text{ms}$ $H_p = 50$, $H_u = 50$		THD with $T_s = 0.2\,\text{ms}$ $H_p = 100$, $H_u = 100$		THD with $T_s = 0.1\,\text{ms}$ $H_p = 200$, $H_u = 200$	
State limit	sparse	dense	sparse	dense	sparse	dense
$\pm$ inf A	0.123 %	0.124 %	0.021 %	0.030 %	0.149 %	0.006 %
± 8 A	0.123 %	0.124 %	0.016 %	0.031 %	0.229 %	0.009 %
± 6 A	0.122 %	0.101 %	0.005 %	0.031 %	0.390 %	0.011 %
± 4 A	0.121 %	0.124 %	0.014 %	0.032 %	0.695 %	0.018 %
± 2 A	0.117 %	0.125 %	0.075 %	0.036 %	1.596 %	0.028 %
± 1 A	0.109 %	0.125 %	0.035 %	0.042 %	3.289 %	0.054 %
average solving time	0.17 ms	1.18 ms	0.33 ms	5.24 ms	0.58 ms	29.5 ms

by a factor of ten. This result concurs with the assumption, that solving sparse formulated MPC QP optimization problems with comparably large prediction horizons and a small number of states perform better than their condensed formulated counterpart as outlined in section 3-2-1.

When analysing the evolution of the THD for longer simulation times, some solutions for the condensed problem formulation seem to take an unusual long time until a steady compensation current is found, that does not increase or decrease the THD further. Figure 4-12 shows THD values calculated at the beginning of each period. The simulations are set up with identical parameters, with the only difference, that the feeder line current i_{f1} is compensated by solutions obtained by the condensed problem, while i_{f2} is obtained by solving the sparse problem. Both solutions find compensations, that lead to a THD of about 0.03 %, but the solution of the condensed problem changes with every period, finding even solutions which lead to a feeder line current THD of below 0.01 %, but then returns to "worse" solutions. This development can only be observed with solutions obtained from condensed problem formulations. Sparse problem solutions tend to reduce the THD right from the first period, only varying slightly for a small number of periods.

Although further investigation of the numerical properties of this effect is needed, an indication for the cause of this effect could lie in the changed structure of the controller itself, when using the sparse problem formulation. Since not input differences are computed but directly the input, the controller does not include a discrete-time

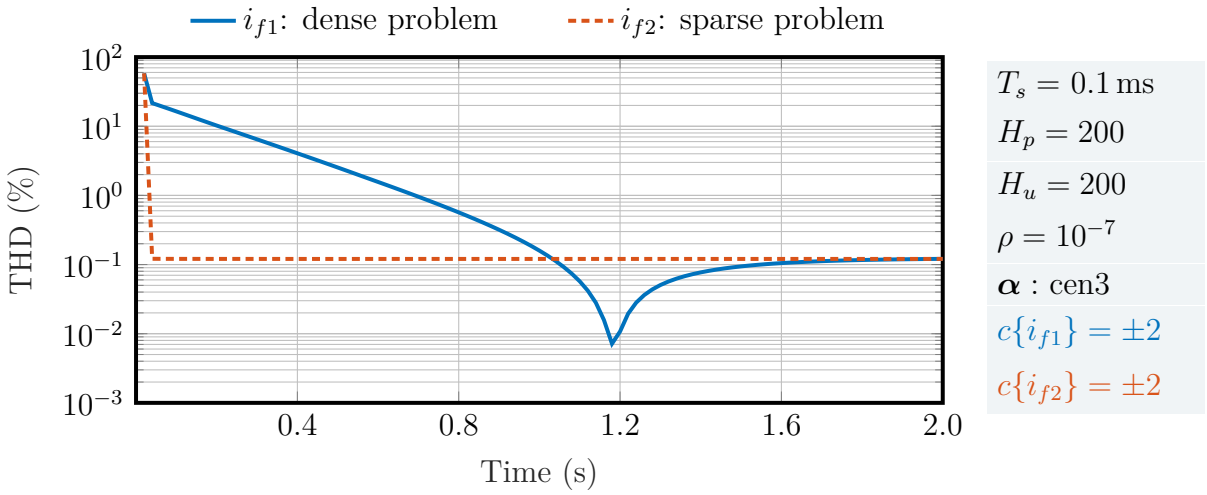

Figure 4-12: Evolution of the THD for the compensation solution using condensed and sparse problem formulations.

integrator like the controller using the condensed problem formulation. Figure 4-13 shows the block diagram of this reduced controller structure. From this block diagram it is apparent, that without the discrete-time integrator the solution of the optimal input is also not dependent on the last input any more. Each solution is disconnected from the previous solution in the sense, that only measured disturbances and the initial state contribute to the solution, it does not matter by which trajectory the initial state is achieved. This allows for a wider set of solutions, which could be an advantage for LSSS MPC optimization problems that directly solve the optimal input.

Another benefit that comes with the implication, that the solution is not tied to the tra-

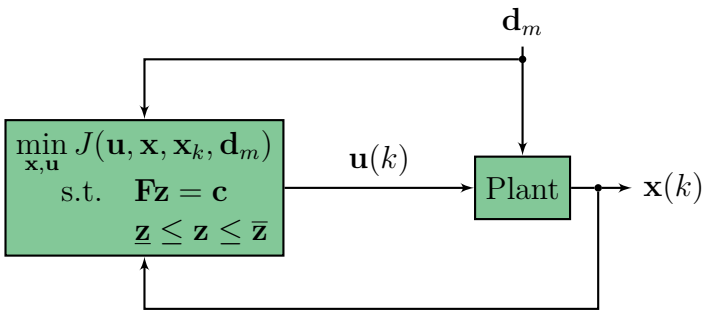

Figure 4-13: Block diagramm of the constrained LSSS MPC controller using sparse problem formulation.

jectory of the initial state, is the possibility to apply the standard RHC strategy instead of the periodic RHC strategy. As stated in the work that introduced the LSSS MPC concept, [21], with the traditional RHC, the optimal input found by solving the optimization problem belongs to different sine waves with each solving step, leading to non-sinusoidal state shapes using this strategy. This statement must hold true, let alone because with each solving step an approximation error is induced into the solution. However, when directly computing the the optimal input and disregarding the state trajectory, this relaxed problem statement will still produce sinusoidal state shapes with only slightly worse compensation results as can be seen in the simulation results of figure 4-14. The THD of the compensated feeder line current is 0.21 %, which is higher than the THD of 0.016 % using a periodic RHC strategy as shown in table 4-2, but still this is a satisfactory compensation result.

The simulation setup is slightly changed when applying the RHC strategy, such that the vector of measured disturbances is initialized with zeros, since no measurements are available. With each simulation step, the vector of measured disturbances is updated. In figure 4-14 it can clearly be observed, that the controller tries to adjust the state to

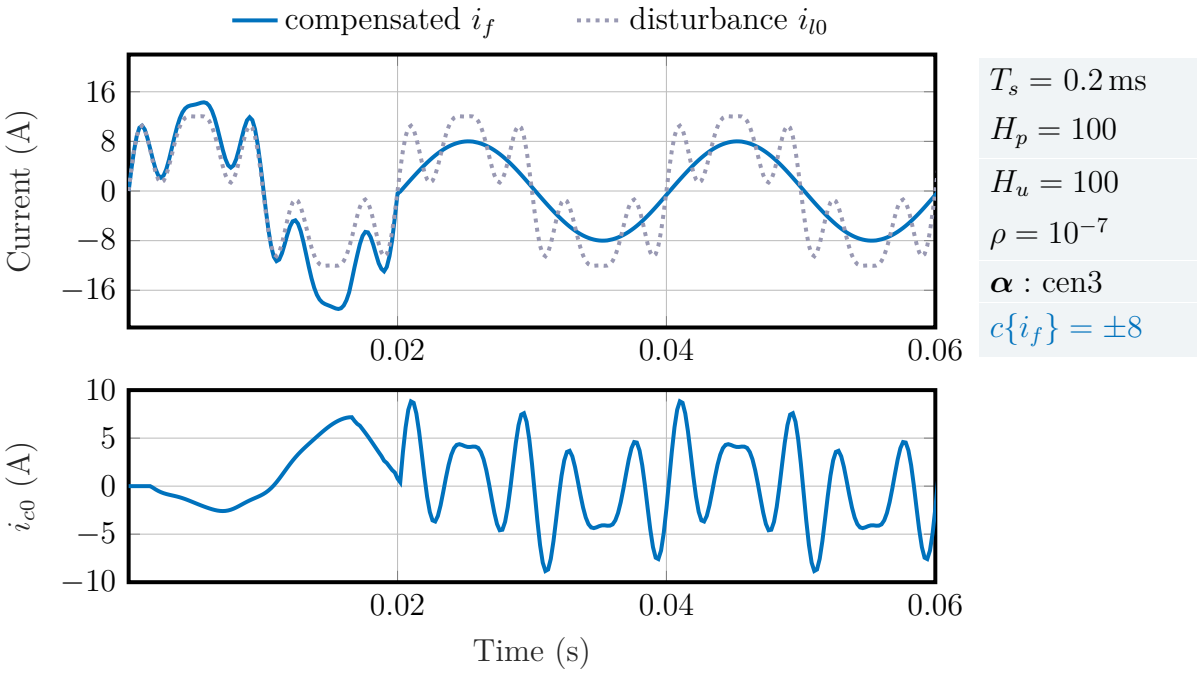

Figure 4-14: Compensation of harmonic load currents with constrained LSSS MPC using the RHC strategy. The upper plot shows the feeder line current i_f, the lower plot shows the compensation current i_{c0}.

the sinusoidal shape with each step right from the beginning. Only when one full period of measured disturbances is available at $t = 0.02\,\mathrm{s}$, a good compensation result can be achieved. When applying a periodic RHC strategy in contrast, the method resembles an open-loop control strategy, where a control input is not updated by current state or output measurements each sampling step. Instead only at the beginning of each period a state update is applied. Figure 4-15 shows the compensation progress in terms of feeder line current distortion, where the THD is calculated at every sampling step using a moving window strategy with a window size $\tau = \frac{1}{fT_s}$. While the THD of i_{f1} only decreases until a steady state compensation input is found, the THD of i_{f2} seems to describe a decaying oscillation as shown in figure 4-16. Although these oscillations are small in value, they give a valuable indication to the numerical properties of the periodic RHC strategy, which is only able to find a new optimal input at the beginning of each period.

An important advantage of the periodic RHC compared to the traditional RHC strategy is the fast computation time. For a frequency of 50 Hz, the optimal input vector for one whole period must be calculated in less than 20 ms, which is an achievable time considering the average computing time results laid out in table 4-2. Only condensed formulated optimization problems with prediction horizons larger than $H_p = 100$ seem to violate this timing restriction. If a traditional RHC strategy is applied, the computing time restriction is tightened, since a new input must be available at each time step. With a discretization of 100 samples per 50 Hz period, each input has to be calculated

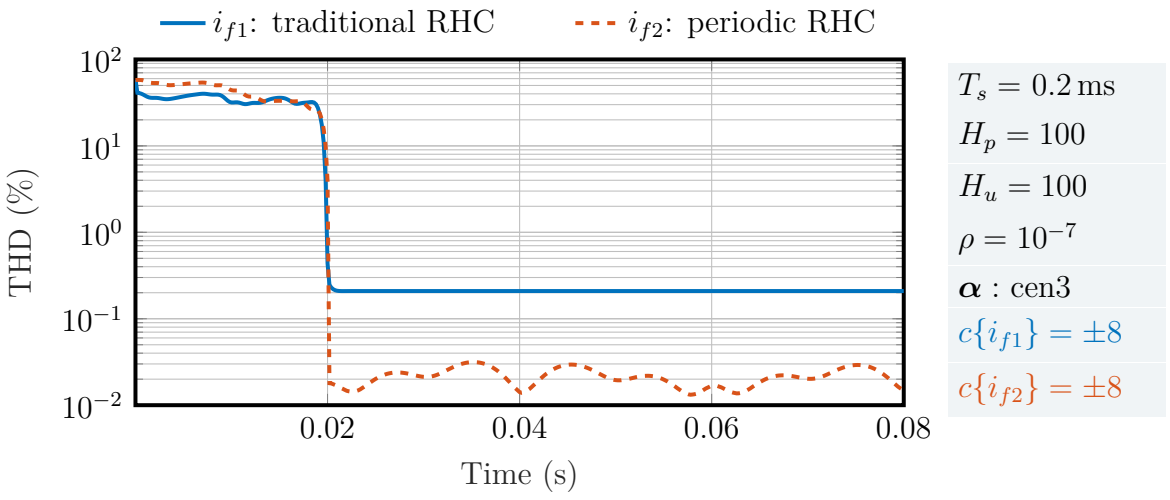

Figure 4-15: Reduction of THD by using constrained LSSS MPC with both periodic RHC and traditional RHC strategies. The THD is measured at every sampling step using a moving window strategy.

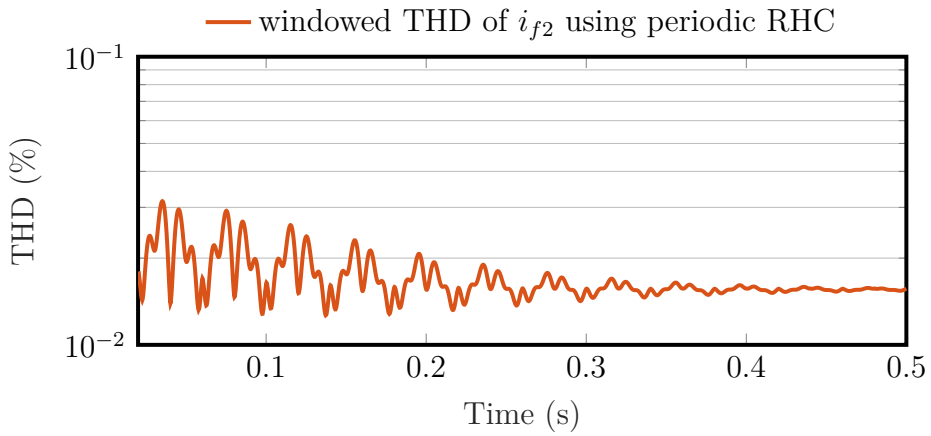

Figure 4-16: Oscillating THD, which is obtained when applying the periodic RHC strategy for compensation.

within 0.2 ms. Although sparse formulations can be computed faster, this timing specification can only be met with small prediction horizons at the expense of approximation accuracy. Yet when applying the traditional RHC strategy, the prediction horizon is no longer tied to the sampling interval T_s as outlined in section 3-4-2. Simulations indeed prove, that with the RHC strategy prediction horizons of down to half the number of samples per 50 Hz period are capable of finding an optimal input solution to compensate disturbances.

Table 4-3 summarizes the results for simulation runs to compensate nonlinear current disturbances by using a sparse problem formulation with the RHC strategy. The state constraints are set to ± 8 A for every simulation and central numerical approximation with three coefficients is used to build up the shape matrix. In the table, t_{solv} denotes the average computing time to find the optimal input and t_{max} denotes the timing restriction, i.e. the maximum allowed time to compute the solution. Parameter settings that violate the timing requirement are highlighted in red. A compensation of nonlinear current disturbances to about 1 % THD is possible using only allowed parameter settings.

Another advantage in using smaller prediction horizons is the ability to recover from disturbance changes faster. Assuming the disturbance changes abruptly at time t_{change}, only after the vector of measured disturbances is fully updated with the information of the new disturbance, a correct compensation current can be computed. With H_p reduced to half a period, also half a period of previous measured disturbances are needed for solving the optimization problem, so that after half a period the new measured disturbance can correctly be compensated.

Table 4-3: Simulations results for compensating nonlinear current disturbances using constrained LSSS MPC with RHC strategy using different parameter settings.

	Simulation parameter							
samples per period	50	50	70	70	90	90	100	100
H_p	50	25	70	35	45	45	50	50
ρ	$9 \cdot 10^{-8}$	$9 \cdot 10^{-8}$	$7 \cdot 10^{-8}$	$7 \cdot 10^{-8}$	$7 \cdot 10^{-8}$	$8 \cdot 10^{-8}$	$8 \cdot 10^{-8}$	$9 \cdot 10^{-8}$
t_{solv}	0.25 ms	0.15 ms	0.39 ms	0.22 ms	0.37 ms	0.16 ms	0.29 ms	0.29 ms
t_{max}	0.4 ms	0.4 ms	0.29 ms	0.29 ms	0.22 ms	0.22 ms	0.2 ms	0.2 ms
	Compensated feeder line current THD							
THD	0.83 %	0.84 %	0.28 %	0.98 %	0.23 %	1.65 %	1.0 %	0.26 %

Figure 4-17 shows the results of a load compensation simulation, where due to a load change at $t_{change} = 90\,\text{ms}$ the disturbance abruptly changes to

$$i_{l0} = 15\sin(\omega_f t + \frac{\pi}{5}) + 4\sin(5\,\omega_f t + \frac{\pi}{5}) + 2\sin(7\,\omega_f t + \frac{\pi}{5})\,. \tag{4-18}$$

The progress of the disturbance is shown in the bottom plot of figure 4-17. For this simulation a sampling interval of $T_s = 0.2\,\text{ms}$ is used, other simulation parameters are denoted in the annotation box between the upper and the mid plot. All simulations use the RHC strategy. The upper plot shows the compensation with a prediction horizon of $H_p = 50$, which matches half the number of samples per period. As can be seen, after 10 ms, i.e. half a period, the disturbance is compensated. The mid plot on the other hand uses a prediction horizon $H_p = 100$, matching the number of samples per period, all other simulation parameters are kept the same. Only after one full period the disturbance signal is compensated.

4-3-3 Limitations

As it is shown in the previous section, applying constraints to the LSSS MPC improves the control strategy and is even possible to relax some restraints to the concept. However, certain limitations still exist. One important drawback is the need to obtain a good measured disturbance signal. In the more realistic case, that the disturbance measurements are afflicted with noise, the controller does not give satisfying compensation results. Figure 4-18 shows the simulation of nonlinear load current compensation

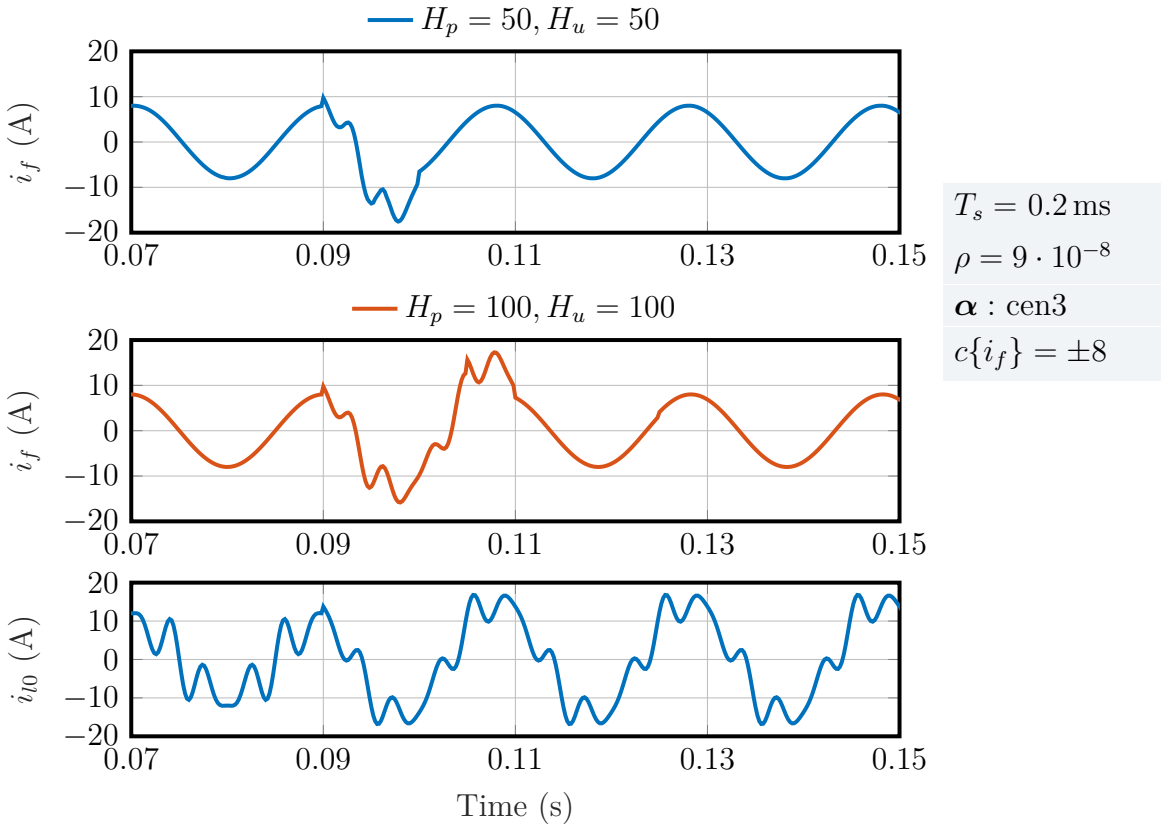

Figure 4-17: Nonlinear load compensation with changing disturbance i_{l0} at $t_{change} = 90\,\mathrm{ms}$. The plots show simulations results using a RHC strategy. The prediction horizon in the top plot is set to half the number of samples per period, the prediction horizon in the mid plot is set to the number of samples per period.

when Gaussian distributed white noise with a variance of $\sigma^2 = 0.25$ is added to the disturbance measurements.

It is apparent, that the compensated feeder line current i_f is very noisy. Considering the decibel scaled signal to noise ratio (SNR), which is defined as

$$\mathrm{SNR} = 20 \log_{10} \frac{\hat{A}_{signal}}{\hat{A}_{noise}}, \tag{4-19}$$

where $\hat{A}_{signal}$ denotes the RMS amplitude of the signal and $\hat{A}_{noise}$ denotes the RMS amplitude of the noise, [40], the analysis shows, that the noise entering the controller through the disturbance measurement is amplified. For the disturbance signal shown in the example the SNR is 29.3 dB, while the SNR of the compensated feeder line current

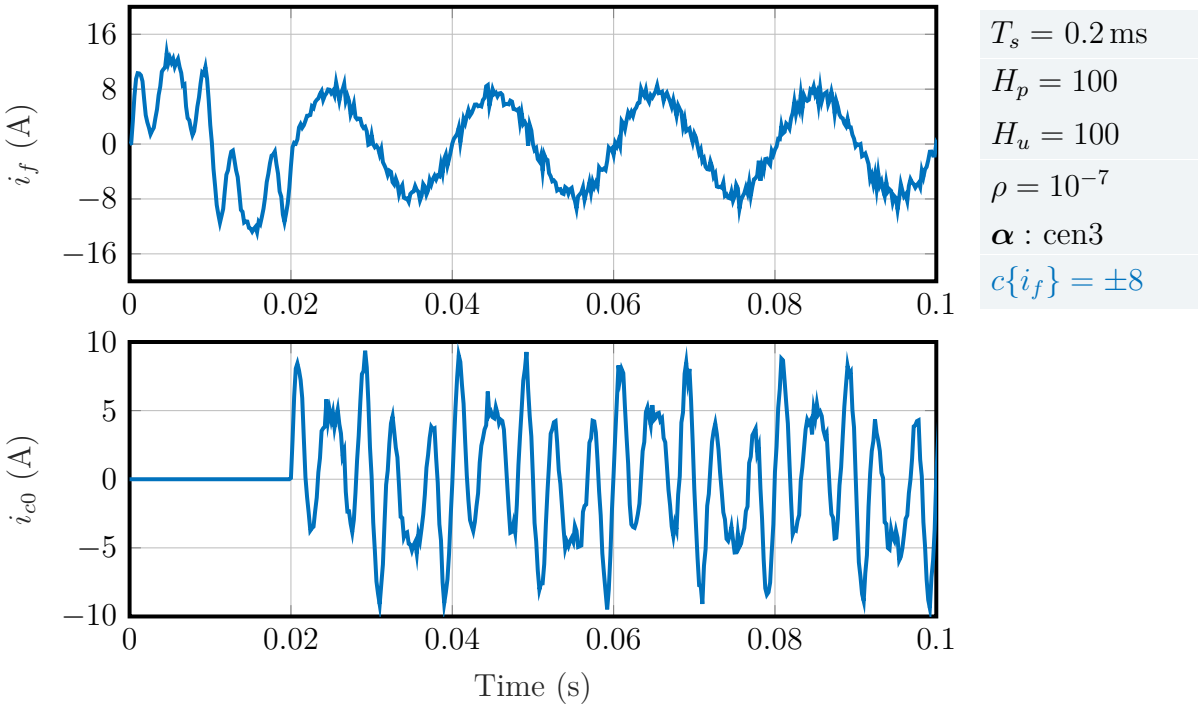

Figure 4-18: Compensating nonlinear load currents with noisy disturbance measurement.

is 14.7 dB, i.e. the ratio between signal and noise is shifted towards a higher noise share. The variance of the compensated feeder line current also is higher than the variance of the noise itself, which can be seen by analysing the distribution of the extracted the noise of the feeder line current with

$$i_{f,noise} = i_{f,clean} - i_f\,, \tag{4-20}$$

where $i_{f,clean}$ denotes the compensated feeder line current, if no measurement noise is applied. In figure 4-19 a histogram comparing the noise of the feeder line current and the disturbance current normalized by their probability density

$$f(x|\sigma^2) = \frac{1}{\sqrt{2\pi\sigma^2}}\, e^{-\frac{x^2}{2\sigma^2}}, \tag{4-21}$$

with fitted probability density curves is shown. The variance increases from $\sigma^2 = 0.25$ for the disturbance noise to $\sigma^2 = 0.64$ for the feeder line current noise, hence the values of the noisy feeder line current are more scattered than the values of the noisy disturbance.

The LSSS MPC always uses the stored measured disturbances of the last period to compute the optimal input, but since the disturbance is different by the time the input

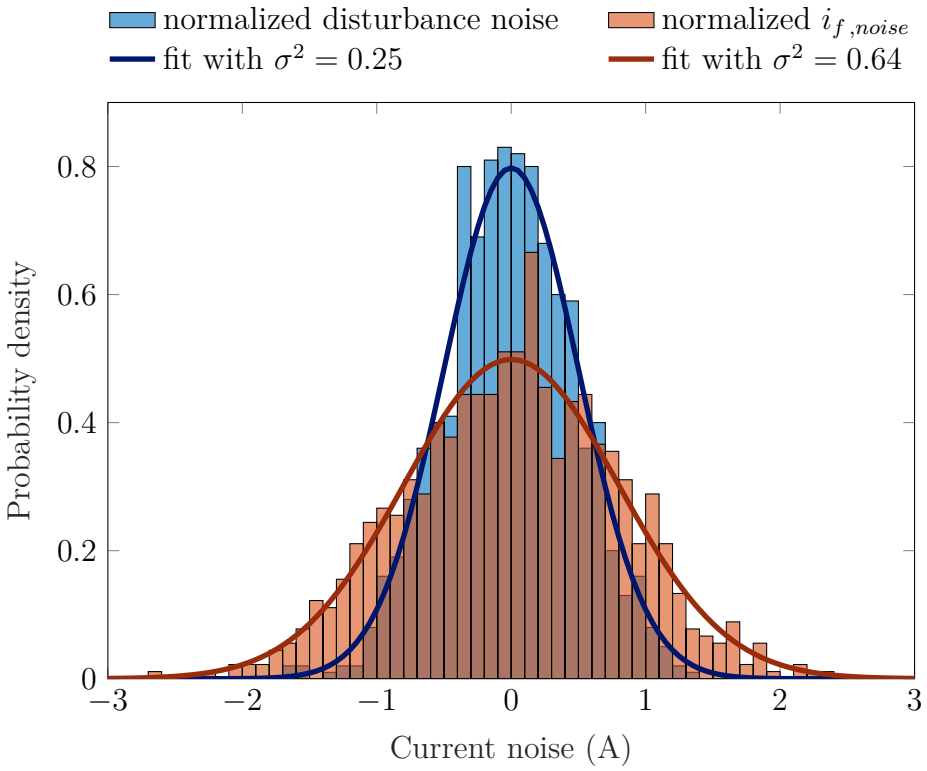

Figure 4-19: Histogram showing the variance increase of the noise.

is applied, the state of the plant will not advance as predicted. Using a stochastic estimator like a Kalman filter as an observer to estimate the exact measured disturbances could improve the performance of the LSSS MPC, so that noise does not get amplified.

Chapter 5

Active Power Filter Simulation

To showcase the possibilities of the constrained linear state signal shaping (LSSS) model predictive control (MPC) as controller for an active power filter (APF), the simulation of a more refined model using MATLAB SIMULINK is developed. The constrained LSSS MPC is used to compute the compensation current in order to cancel out distorted currents drawn from rectifiers, which are connected to each phase. Additionally, a simulation of a classical APF using the instantaneous reactive power (IRP) theory to estimate the reference signal is set up to compare the performance of the LSSS MPC to the IRP APF.

5-1 Simulation Framework

Based on the three phase three node grid example shown in figure 2-5, a grid model as depicted in figure 5-1 is implemented as MATLAB SIMULINK model using the Simscape Power Systems library. The model includes feeder line transmission resistances R_f to express transmission losses, which exist in real electric power transmission networks, [6]. The nonlinear load is modelled by a bridge rectifier using a smoothing capacitor C_{DC}, which supplies a linear load R_l with direct current (DC) voltage. The model parameters are summarized in table 5-1.

A fixed-step solver using the first order Euler method is used to simulate the model. The classical IRP APF uses a hysteresis band controller to control a voltage source converter (VSC), which generates the compensation currents based on switching signals. The upper and lower limits for the hysteresis band controller are set to $\pm 0.01\,\mathrm{A}$. Since the fundamental sampling time confines the maximal switching frequency, it is set

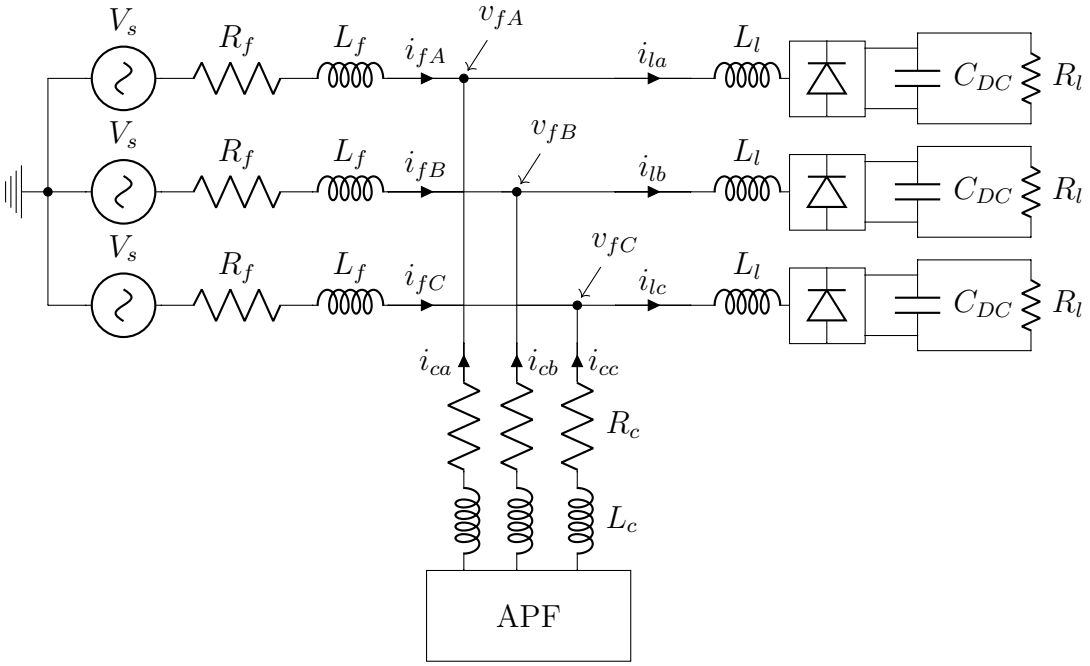

Figure 5-1: Three-phase three-node grid model.

to 0.01 ms, which accounts for a maximal switching frequency of 100 kHz. This is a particular high frequency, but it is intentionally chosen to achieve a switching ripple as small as possible. The grid model utilized for the MPC on the other hand uses an ideal current source. Controlling a VSC directly by an MPC controller is possible as mentioned in section 4-2, but requires additional modelling effort. With the limitation of using ideal current sources, smaller switching frequencies would result in an unfair advantage for the LSSS MPC, since current sources are able to output currents without any switching ripple.

Not only the compensation for one static load is analysed, but also the transient behaviour and the possibility to adapt to load changes for both the LSSS MPC and the IRP APF is assessed. For this, the linear load R_l connected to the DC side of the rectifier changes from $R_l = 100\,\Omega$ to $9\,\Omega$ after 0.5 s and to $2\,\Omega$ after 1 s after the simulation started. Figure 5-2 shows simulation of the grid model without compensation. The upper plot shows the resulting feeder line current, the lower plot shows the point of common coupling (PCC) voltage. As can be seen, with increasing currents on the feeder line the PCC voltage decreases due to increasing voltage drops on the transmission line impedance. This effect is undesired, since this means, that loads are not sufficiently granted with the needed root mean square (RMS) supply voltage of 230 V. The total harmonic distortion (THD) of the feeder line current and the supply voltage are shown

Table 5-1: Simulation parameters.

Parameter	Symbol	Value
Sampling time IRP APF	T_{s1}	$1 \times 10^{-5}\,\mathrm{s}$
Sampling time LSSS MPC APF	T_{s2}	$2 \times 10^{-4}\,\mathrm{s}$
Phase-to-ground RMS voltage	V_s	$230\,\mathrm{V}$
Grid frequency	f	$50\,\mathrm{Hz}$
Feeder line resistance	R_f	$1\,\Omega$
Feeder line inductance	L_f	$0.01\,\mathrm{mH}$
Filter coupling resistance	R_c	$0.001\,\Omega$
Filter coupling inductance	L_c	$3.50\,\mathrm{mH}$
VSC DC Link voltage	V_{DC}	$800\,\mathrm{V}$
AC load coupling inductance	L_l	$2\,\mathrm{mH}$
DC smoothing capacitor	C_{DC}	$0.68\,\mathrm{mF}$
LSSS MPC input weighting factor	ρ	10^{-7}

in figure 5-3 in the upper plot and lower plot respectively. While the THD decreases for the feeder line current, because with increasing amplitude the waveform resembles a sine wave more and more, the PCC voltage THD increases from 1.9 % initially to 9 % at $t = 1.5\,\mathrm{s}$.

The SIMULINK grid model consists of three phases, but only one phase is connected to the LSSS MPC since the grid equivalent model used in the MPC only represents single phase system dynamics. A more complex equivalent model that also adds dynamics between phases would be needed to implement a three phase LSSS MPC, which exceeds the scope of this thesis. Therefore the whole three phase grid model is simulated, but only the first phase is considered for analysis and comparison. All model files can be found on the the CD accompanying this thesis.

5-2 Harmonic Current Compensation by Linear State Signal Shaping MPC

The LSSS MPC uses the sparse formulation to solve the optimization problem using central numerical approximation with three coefficients to compose the shape matrix. A figure of the top level of the SIMULINK model can be found in appendix A-1. The receding horizon control (RHC) strategy is applied because it adapts better to nonlinear

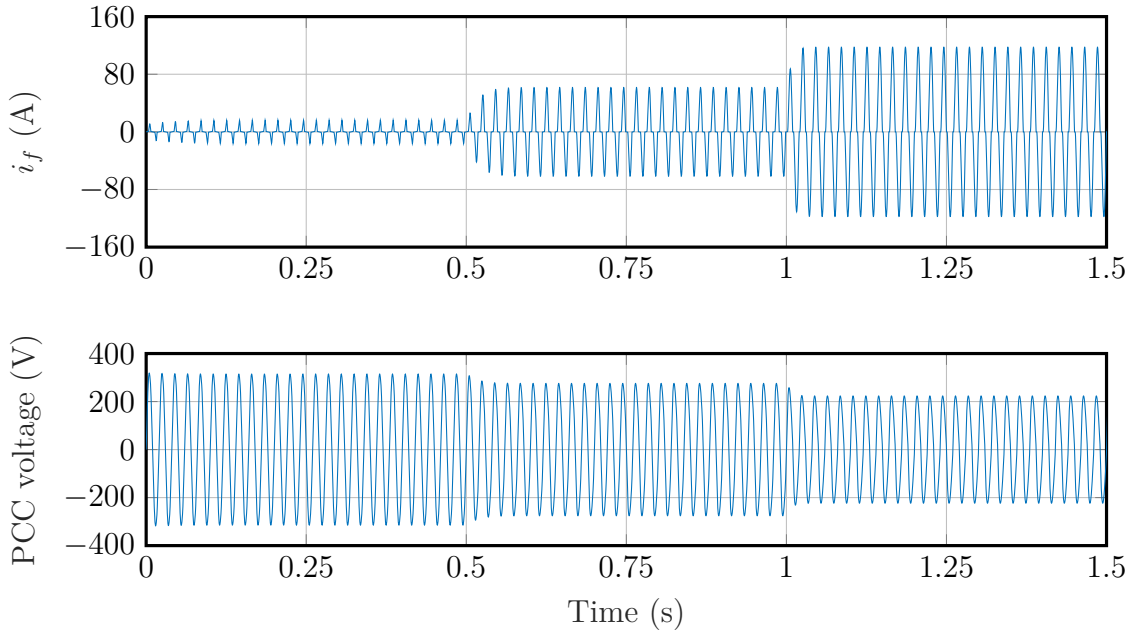

Figure 5-2: Three phase three node grid simulation showing uncompensated distorted currents drawn from varying nonlinear loads. The upper plot shows the resulting feeder line current, the lower plot shows the decreasing PCC voltage.

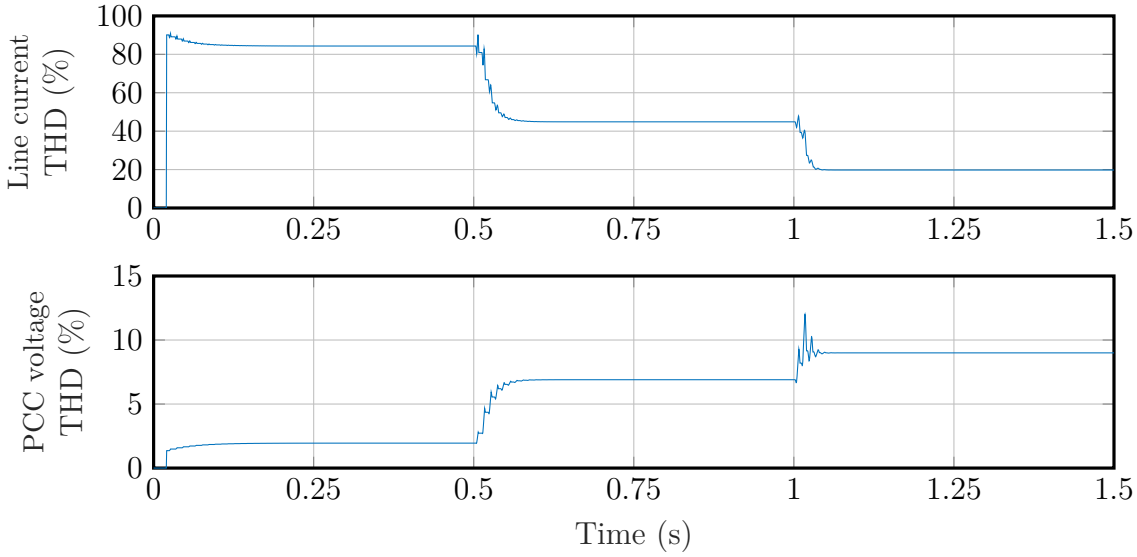

Figure 5-3: THD of feeder line current (upper plot) and supply voltage (lower plot).

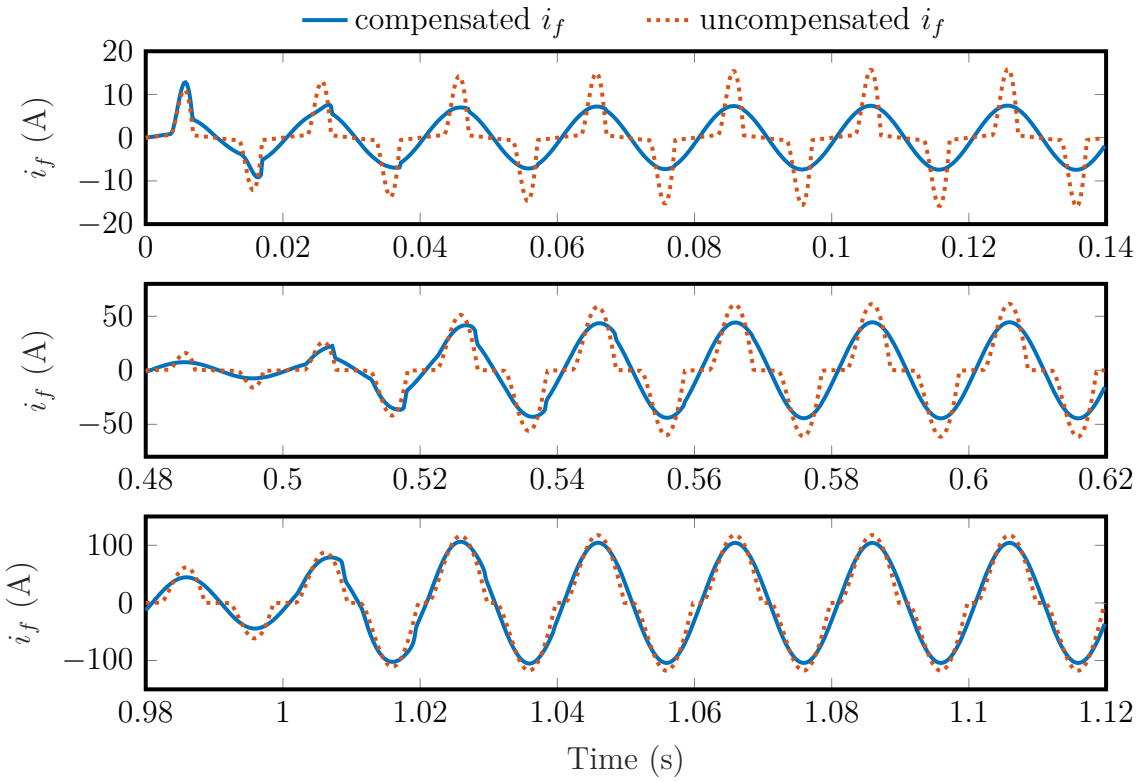

Figure 5-4: Compensated feeder line current of the first phase using the LSSS MPC APF. Parameters for the MPC are $T_{s2} = 0.2\,\text{ms}$, $H_p = 50$, $H_u = 50$, $\rho = 10^{-7}$, central numerical approximation using 3 coefficients, no state constraints. Upper plot: First load scenario with $R_l = 100\,\Omega$. Mid plot: Second load scenario with $R_l = 9\,\Omega$. Bottom plot: Third load scenario with $R_l = 2\,\Omega$.

load disturbance changes when reducing the prediction horizon to half the number of samples per period as outlined in section 4-3-2. Figure 5-4 shows the results of the simulation, when no constraints on the feeder line current are applied. In the upper plot the first load scenario with $R_l = 100\,\Omega$ is active. After a few periods the feeder line current is able to adjust to a sinusoidal shape because a suitable compensation current is injected into the PCC. The LSSS MPC APF is also able to react to load changes, as can be seen in the mid and bottom plot, where the feeder line current is distorted quite heavily at the time of the load step, but the THD quickly decreases to low values, which are summarized in table 5-2 at the end of the section.

The compensation performance regarding the THD is satisfactory, but still a drop of PCC voltage exists as can be seen in table 5-2. The RMS voltage $\hat{V}_f$ at the PCC decreases from initially 226.9 V at the first load scenario to 201.0 V with the load step

at $t = 0.5\,\mathrm{s}$ to $161.8\,\mathrm{V}$ with the last load step at $t = 1\,\mathrm{s}$.

A great advantage of APF over passive filters is the capability of not only compensating distorted currents, but also being able to provide supply voltage stabilization as described in section 2-2-1. Simulation results show, that the LSSS MPC also is able to support the PCC voltage when state constraints on the feeder line currents are applied.

Figure 5-5 shows the compensation results on the constrained LSSS MPC with state limits on the feeder line current of $\pm 20\,\mathrm{A}$. While the top plot is equal to the top plot of figure 5-4, since the constraints are not active, the effect of the current constraints can be seen in the mid and bottom plots. When the load steps at $t = 0.5\,\mathrm{s}$ and $t = 1\,\mathrm{s}$ occur, the feeder line current takes a little longer to achieve a sinusoidal shape than without state constraints, but the current limit is met. Since the overall feeder line current is reduced, the voltage drop on the transmission impedances also is lower, which allows

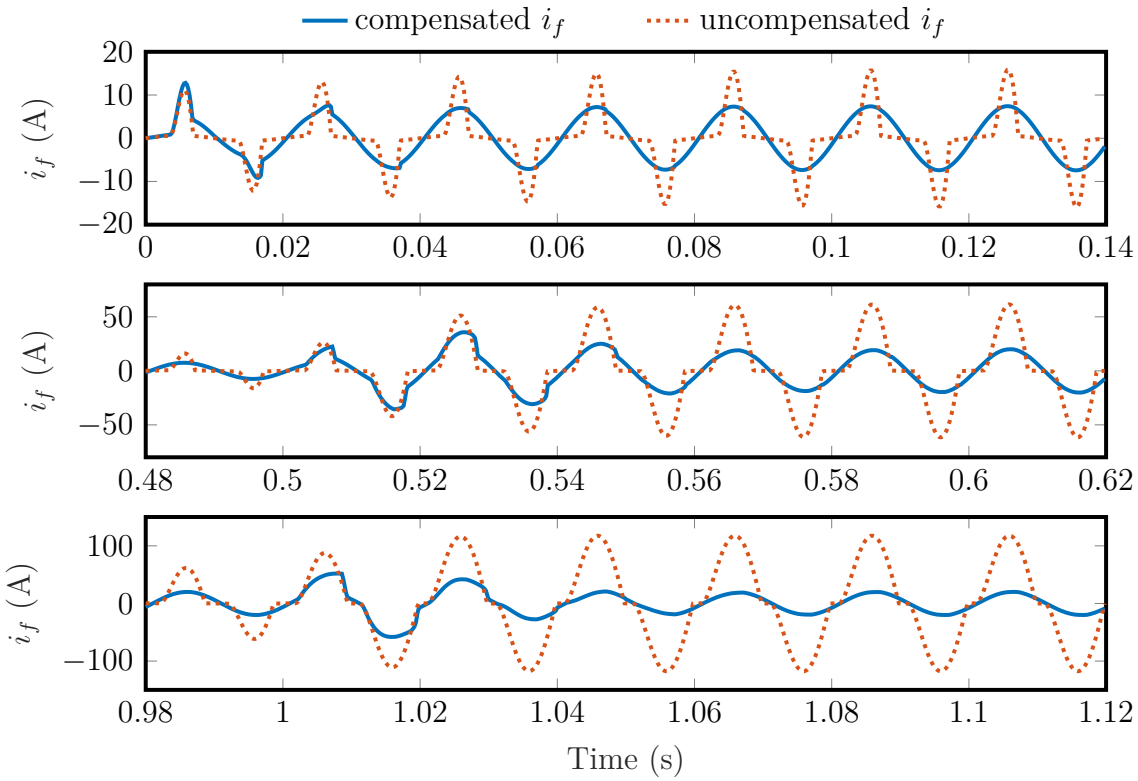

Figure 5-5: Compensated feeder line current of the first phase using the constrained LSSS MPC APF. Parameters for the MPC are $T_{s2} = 0.2\,\mathrm{ms}$, $H_p = 50$, $H_u = 50$, $\rho = 10^{-7}$, central numerical approximation using 3 coefficients, limits on the feeder line current $c\{i_f\} = \pm 20\,\mathrm{A}$. Upper plot: First load scenario with $R_l = 100\,\Omega$. Mid plot: Second load scenario with $R_l = 9\,\Omega$. Bottom plot: Third load scenario with $R_l = 2\,\Omega$.

Table 5-2: Comparison of feeder line current THD, PCC voltage THD and PCC RMS voltages for uncompensated and compensated LSSS MPC APF operation at different load scenarios.

		Uncompensated	Compensated, $c\{i_f\} = \pm\inf$	Compensated $c\{i_f\} = \pm 20$
t = 0.48 s	i_f THD	84.5 %	0.18 %	0.18 %
	v_f THD	1.95 %	0.004 %	0.004 %
	$\hat{V}_f$	226.9 V	226.9 V	226.9 V
t = 0.98 s	i_f THD	44.9 %	0.18 %	0.18 %
	v_f THD	6.9 %	0.004 %	0.004 %
	$\hat{V}_f$	201.4 V	201.0 V	217.5 V
t = 1.48 s	i_f THD	19.77 %	0.11 %	0.36 %
	v_f THD	9.00 %	0.017 %	0.024 %
	$\hat{V}_f$	162.1 V	161.8 V	217.9 V

for higher PCC voltages.

Table 5-2 summarizes the compensation results for the unconstrained as well as the constrained LSSS MPC. The THD of the feeder line current i_f and the PCC voltage v_f of the unconstrained case differ only marginally when state constraints are applied. The RMS PCC voltage $\hat{V}_f$ on the other hand is stabilized, when limiting the feeder line current, because the currents are mainly exchanged between load and APF, therefore reducing the currents on the transmission line. This also means, that the APF must be installed close to heavy loads, if the power filter should be operated in PCC voltage stabilizing mode.

5-3 Comparison with a Classic Harmonic Compensation Strategy

The block diagram of the IRP APF Simulink model can be found in appendix A-2. The classical APF is designed to provide harmonic compensation as well as PCC voltage stabilization as outlined in section 2-2-1. For this the VSC has to be designed according to an assumed PCC voltage drop, such that enough energy can be stored in the DC link capacitor. For the benefit of simplicity, the IRP APF is designed to stabilize the second load scenario with harmonic compensation and suitable PCC voltage compensation best. Techniques to adjust the APF to different loads exist, [46], but designing such a filter goes beyond the scope of this thesis.

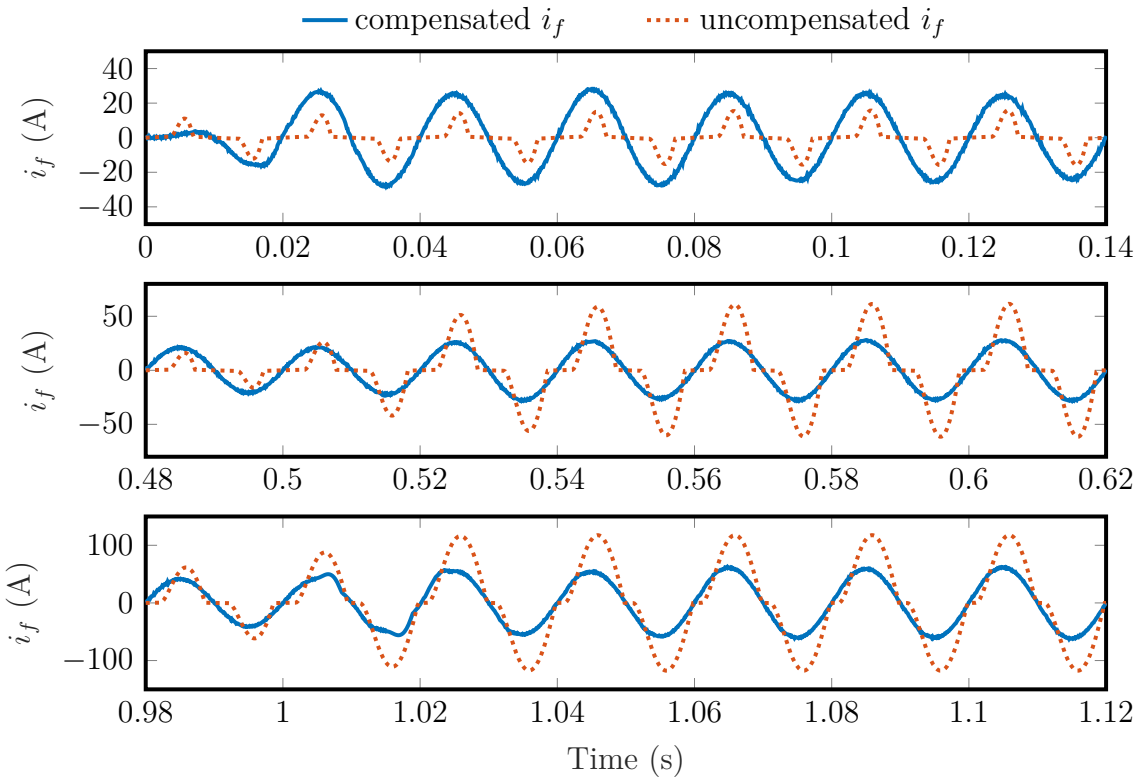

Figure 5-6: Compensated feeder line currents of the first phase using the IRP APF. Upper plot: First load scenario with $R_l = 100\,\Omega$. Mid plot: Second load scenario with $R_l = 9\,\Omega$. Bottom plot: Third load scenario with $R_l = 2\,\Omega$.

Simulation results of the compensation performance of the classical IRP APF using the parameters outlined in section 5-1 are shown in figure 5-6. The feeder line currents for the first load scenario are higher compared to the currents shown in figure 5-5, the maximum current is at 28.5 A compared to 12.8 A with LSSS MPC compensation. This increased current most likely is caused due to the IRP APF being designed for a different load scenario.

The compensation results for the second load scenario with $R_l = 9\,\Omega$ at $t = 0.5\,\text{s}$ until $t = 1\,\text{s}$ are similar to the compensation results of the constrained LSSS MPC, as can be seen in figure 5-7. Noticeable is a phase shift, when comparing both compensation currents and feeder line currents. Recalling the grid model in figure 5-1, a load coupling inductance is modelled to connect the load to the PCC, acting as inductive reactance and therefore causing a phase shift. The IRP APF is capable of compensating this phase shift in contrast to the LSSS MPC, which still is a main drawback of the latter compensation method.

Table 5-3: Compensation results of IRP APF and constrained LSSS MPC APF harmonic compensation.

		Uncompensated	Compensated by IRP APF	Compensated by constrained LSSS MPC
t = 0.48 s	i_f THD	84.5 %	2.90 %	0.18 %
	v_f THD	1.95 %	0.75 %	0.004 %
	$\hat{V}_f$	226.9 V	217.5 V	226.9 V
t = 0.98 s	i_f THD	44.9 %	2.29 %	0.18 %
	v_f THD	6.9 %	0.81 %	0.004 %
	$\hat{V}_f$	201.4 V	216.0 V	217.5 V
t = 1.48 s	i_f THD	19.77 %	1.65 %	0.36 %
	v_f THD	9.00 %	0.87 %	0.024 %
	$\hat{V}_f$	162.1 V	208.2 V	217.9%

In table 5-3 the compensation performance regarding THD reduction and voltage stabilization of the IRP APF and the constrained LSSS MPC APF is compared. Note that the feeder line current THD compensated by the IRP APF has to be higher due to

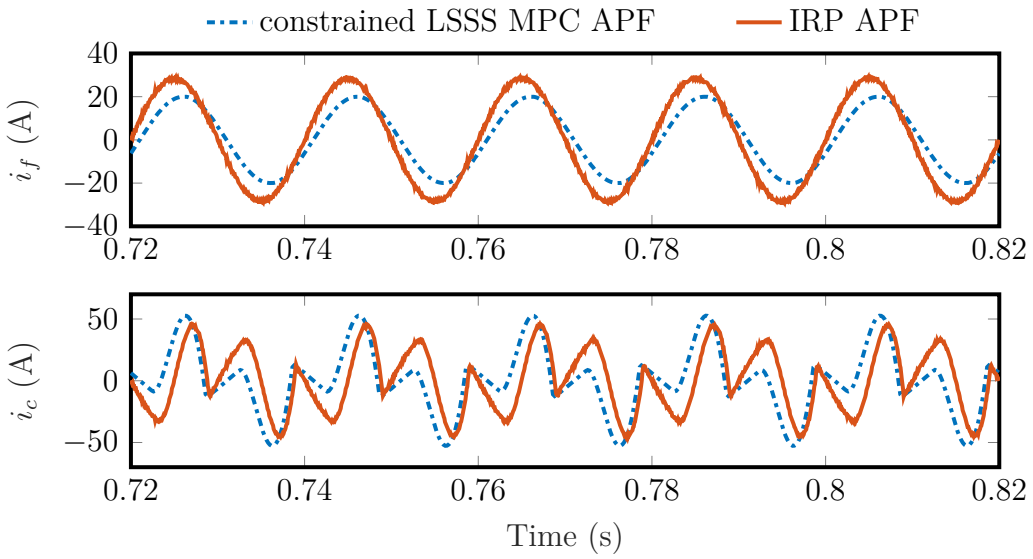

Figure 5-7: Comparison of compensated feeder line current and compensation current of the IRP APF and LSSS MPC compensated nonlinear load. The figure shows the simulation results for the second load scenario with $R_l = 9\,\Omega$

switching ripples of the VSC and therefore should not directly be compared to the results of the LSSS MPC, which is using an ideal current source. Regarding the PCC voltage stabilization, both methods achieve similar results with the constrained LSSS MPC performing slightly better, keeping the RMS PCC voltage above 217 V. With the first load scenario the LSSS MPC even outperforms the IRP APF. While the IRP APF is designed to perform best in the second load scenario, falling behind with different load setups, the LSSS MPC does not need to be adjusted to load changes, which could be an advantage of this method compared to classical concepts.

Still the LSSS MPC needs to be enhanced with the possibility to compensate reactive power to fully be able to replace a classical APF. Including the VSC into the LSSS MPC model and directly computing the switching pattern provides the ability to control the DC link capacitor voltage in a similar way, like it is done with the IRP APF. Reactive power components in the grid will also affect charging and discharging the DC link capacitor, which can be utilized to include reactive power compensation by calculating the energy losses in the capacitor as described in section 2-2-1.

Chapter 6

Conclusion

Maintaining quality in power networks is an important task for providing an efficient and safe energy supply. Ancillary services like harmonic mitigation and reactive power compensation improve the overall power quality and they are in increasing demand due to the challenges that accompany the integration of renewable energy sources into the grid. This thesis presents solutions to enhance the novel linear state signal shaping (LSSS) model predictive control (MPC) technique in such a way, that it could be employed as an active power filter (APF). In section 6-1 the results of this thesis are summarized, concluding with an outlook for future work in section 6-2.

6-1 Summary

The unconstrained LSSS MPC provides a new control scheme that differs from existing MPC implementations by incorporating a desired sinusoidal signal shape into the optimization problem. This controller is able to find an optimal input, so that the states of a plant adopt an undistorted sinusoidal shape, but it lacks the ability to maintain a fixed state signal amplitude magnitude. This thesis shows that applying state constraints to the LSSS MPC not only allows for a stable amplitude, but also the ability to set upper and lower state limits is given. For this, the optimization problem is set up either in a condensed or a sparse optimization problem formulation, which allows the problem to be solved by a numerical quadratic program (QP) solver. Comparisons show that the sparse formulation exhibits superior numerical properties over the condensed problem formulation with faster computation times and the ability to use the traditional receding horizon control (RHC) strategy instead of being restricted to periodic RHC.

The developed concepts for controlling the state signal amplitude are applied to compensate currents drawn from nonlinear loads, which is the main task of an APF. Simulation results of an electrical three phase grid connected to a nonlinear load show that the constrained LSSS MPC is able to provide simultaneous harmonic compensation and point of common coupling (PCC) voltage stabilization. In direct comparison to a proven classical APF, the LSSS MPC achieves equally good harmonic compensation results. In contrast to the classical concept, the constrained LSSS MPC also is able to adjust to load changes.

6-2 Outlook

Constraining the states of a plant offers the possibility to set upper and lower state limits, but it is not possible to find optimal inputs, that lead to arbitrarily high amplitudes of the state signal. Only if the unconstrained solution offers optimal inputs to increase the state signal amplitude magnitude, the states will possibly reach a sufficiently high value, which then can be constrained to not increase further. This method relies on heuristic tuning of the cost function's weighting factors, which does not offer satisfying predictability of the state trajectory. Formulating the cost function in such a way, that it includes information about the state signal root mean square (RMS) addresses this issue, although this would lead to a biquadratic optimization problem with slower projected solving time. Proving convexity of this optimization problem and exploring possibilities to efficiently solve this problem could be steps into the direction of finding a general method to limit the solution space of the LSSS MPC problem. With this, only solutions with a defined amplitude magnitude could be found.

The analysis of Gaussian noise on the measured disturbances show that relying on the assumption, that the disturbances of the last period is equal to the disturbance of the current period, could amplify the noise. Developing a disturbance observer could improve the performance of the LSSS MPC, if the intention is to implement this controller in hardware.

The comparison of the constrained LSSS MPC APF to a classical instantaneous reactive power (IRP) APF shows that the signal shaping controller achieves competitive harmonic compensation results, but it lacks the ability to provide reactive power compensation in it's current state. Enhancing the model of the MPC to include the voltage source converter (VSC), which is used to inject the compensation currents into the grid, could allow to also control the direct current (DC) link capacitor voltage. With this it should be possible to additionally provide reactive power compensation.

Appendix A

Simulink Block Diagrams

This appendix shows the top level block diagrams of implemented controllers in SIMULINK. The complete models can be found on the CD accompanying this thesis.

A-1 Constrained LSSS MPC Active Power Filter

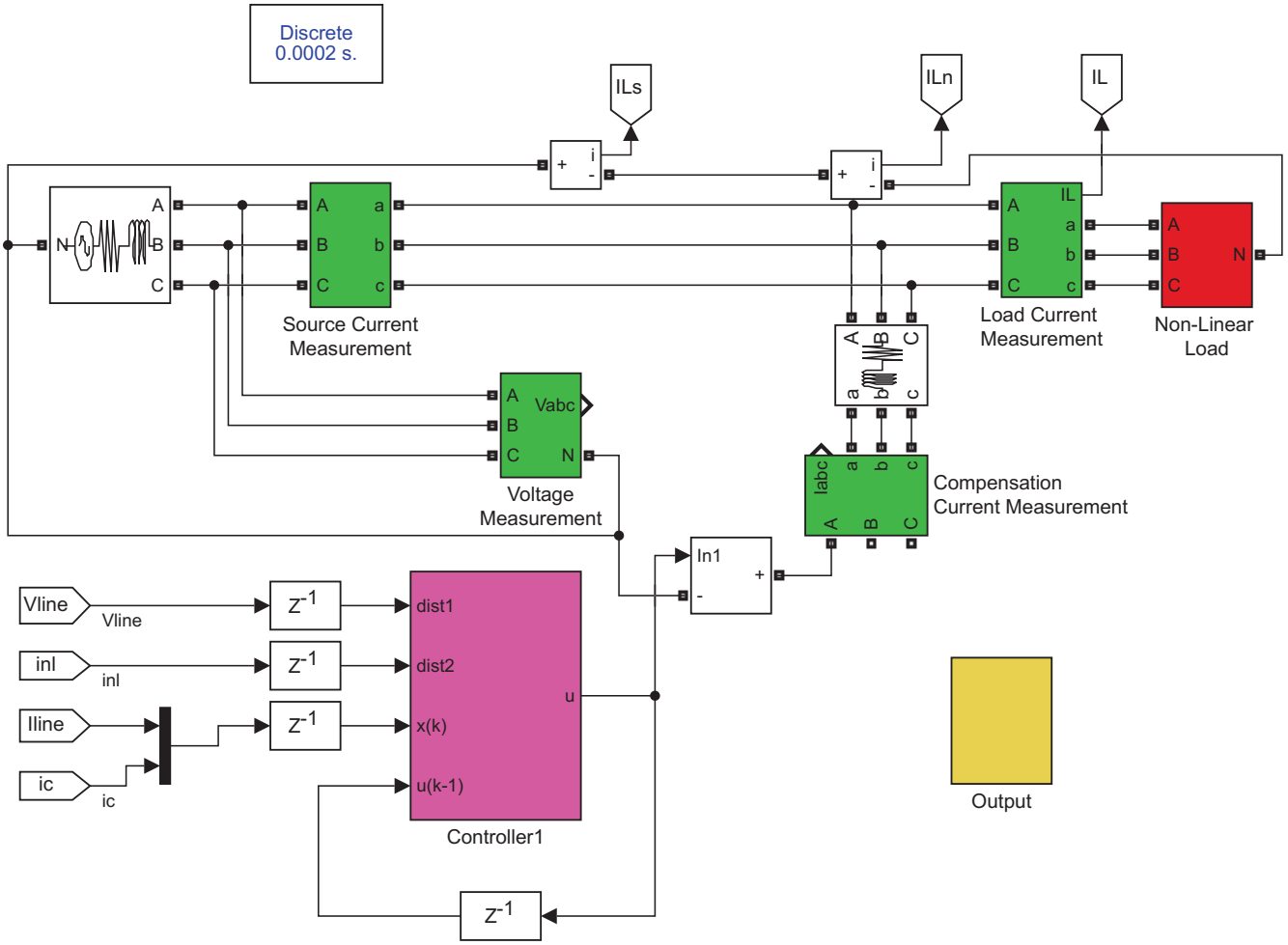

A-2 Instantaneous Reference Frame Active Power Filter

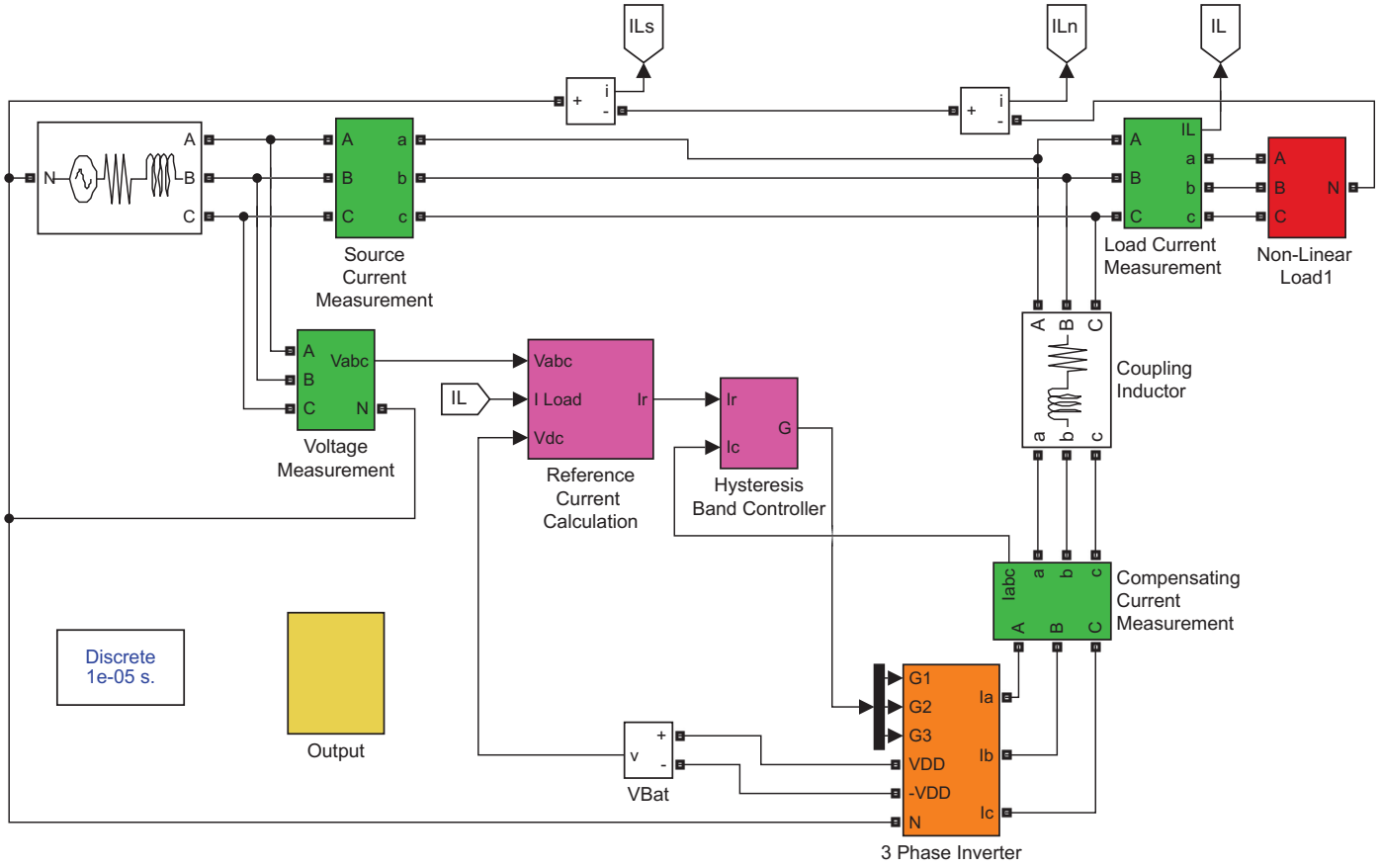

Bibliography

[1] J. Capel and W. Prof. Dr. Beba, "NEW 4.0 Broschüre (PDF) Englisch." http://www.new4-0.de/downloads/, Apr. 2017.

[2] B. Singh, A. Chandra, and K. Al-Haddad, eds., *Power Quality Problems and Mitigation Techniques*. Chichester, United Kingdom: John Wiley & Sons Ltd, Jan. 2015.

[3] S. Elphick, P. Ciufo, V. Smith, and S. Perera, "Summary of the economic impacts of power quality on consumers," in *2015 Australasian Universities Power Engineering Conference (AUPEC)*, pp. 1–6, Sept. 2015.

[4] "Voltage characteristics of electricity supplied by public distribution networks," Standard DIN EN 50160:2011-02, Deutsches Institut für Normung, Feb. 2011.

[5] "Electromagnetic compatibility (EMC) - Part 3-2: Limits - Limits for harmonic current emissions (equipment input current <= 16 A per phase)," Standard IEC 61000-3-2, International Electrotechnical Commission, Jan. 2018.

[6] E. F. Fuchs and M. A. S. Masoum, *Power Quality in Power Systems and Electrical Machines*. Amsterdam: Elsevier, 2015.

[7] F. Blaabjerg, K. Ma, and Y. Yang, "Power Electronics for Renewable Energy Systems - Status and Trends," in *CIPS 2014; 8th International Conference on Integrated Power Electronics Systems*, pp. 1–11, Feb. 2014.

[8] B. Kędra, "Reducing inverter power rating in active power filters using proposed hybrid power filter topology," in *2015 IEEE 15th International Conference on Environment and Electrical Engineering (EEEIC)*, pp. 443–448, June 2015.

[9] C. Lam, W. Choi, M. Wong, and Y. Han, "Adaptive DC-Link Voltage-Controlled Hybrid Active Power Filters for Reactive Power Compensation," *IEEE Transactions on Power Electronics*, vol. 27, pp. 1758–1772, Apr. 2012.

[10] S. Rahmani, A. Hamadi, K. Al-Haddad, and L. A. Dessaint, "A Combination of Shunt Hybrid Power Filter and Thyristor-Controlled Reactor for Power Quality," *IEEE Transactions on Industrial Electronics*, vol. 61, pp. 2152–2164, May 2014.

[11] Q. Liu, L. Peng, Y. Kang, S. Tang, D. Wu, and Y. Qi, "A Novel Design and Optimization Method of an LCL Filter for a Shunt Active Power Filter," *IEEE Transactions on Industrial Electronics*, vol. 61, pp. 4000–4010, Aug. 2014.

[12] S. A. Taher, M. H. Alaee, and Z. D. Arani, "Model predictive control of PV-based shunt active power filter in single phase low voltage grid using conservative power theory," in *2017 8th Power Electronics, Drive Systems Technologies Conference (PEDSTC)*, pp. 253–258, Feb. 2017.

[13] M. H. Alaee, S. A. Taher, and Z. D. Arani, "Improved performance of single-phase shunt active power filter by using conservative power theory and model predictive control," in *2018 9th Annual Power Electronics, Drives Systems and Technologies Conference (PEDSTC)*, pp. 163–168, Feb. 2018.

[14] L. Tarisciotti, A. Formentini, A. Gaeta, M. Degano, P. Zanchetta, R. Rabbeni, and M. Pucci, "Model Predictive Control for Shunt Active Filters With Fixed Switching Frequency," *IEEE Transactions on Industry Applications*, vol. 53, pp. 296–304, Jan. 2017.

[15] K. Antoniewicz, M. Jasiński, and M. P. Kaźmierkowski, "Model predictive control of three-level four-leg flying capacitor converter operating as Shunt Active Power Filter," in *2015 IEEE International Conference on Industrial Technology (ICIT)*, pp. 2288–2294, Mar. 2015.

[16] F. Borrelli, A. Bemporad, and M. Morari, *Predictive Control for Linear and Hybrid Systems*. Cambridge University Press, 1 ed., June 2017.

[17] A. Domahidi, A. U. Zgraggen, M. N. Zeilinger, M. Morari, and C. N. Jones, "Efficient interior point methods for multistage problems arising in receding horizon control," in *2012 IEEE 51st IEEE Conference on Decision and Control (CDC)*, pp. 668–674, Dec. 2012.

[18] P. Patrinos and A. Bemporad, "An Accelerated Dual Gradient-Projection Algorithm for Embedded Linear Model Predictive Control," *IEEE Transactions on Automatic Control*, vol. 59, pp. 18–33, Jan. 2014.

[19] T. V. Dang, K. V. Ling, and J. M. Maciejowski, "Embedded ADMM-based QP solver for MPC with polytopic constraints," in *2015 European Control Conference (ECC)*, pp. 3446–3451, July 2015.

[20] S. Richter, S. Mariéthoz, and M. Morari, "High-speed online MPC based on a fast gradient method applied to power converter control," in *Proceedings of the 2010 American Control Conference*, pp. 4737–4743, June 2010.

[21] C. Cateriano Yáñez, *Model Predictive Ideal Harmonic and Reactive Power Compensation for Fixed Frequency in Distribution Grids*. Master Thesis, University of Applied Sciences, Hamburg, Apr. 2017.

[22] C. Cateriano Yáñez, G. Pangalos, and G. Lichtenberg, "An Approach to linear state Signal Shaping by quadratic Model Predictive Control," in *2018 European Control Conference (ECC)*, (Limassol), June 2016.

[23] H. Akagi, "New trends in active filters for power conditioning," *IEEE Transactions on Industry Applications*, vol. 32, pp. 1312–1322, Nov. 1996.

[24] M. El-Habrouk, M. K. Darwish, and P. Mehta, "Active power filters: A review," *IEE Proceedings - Electric Power Applications*, vol. 147, pp. 403–413, Sept. 2000.

[25] J. K. Phipps, "A transfer function approach to harmonic filter design," in *Industry Applications Society 42nd Annual Petroleum and Chemical Industry Conference*, pp. 175–186, Sept. 1995.

[26] "IEEE Standard Definitions for the Measurement of Electric Power Quantities Under Sinusoidal, Nonsinusoidal, Balanced, or Unbalanced Conditions," Standard IEEE 1459-2010, Institute of Electrical and Electronics Engineers, Mar. 2010.

[27] "Electromagnetic compatibility (EMC) - Part 1: General - Section 1: Application and interpretation of fundamental definitions and terms," Standard IEC 61000-1-1, International Electrotechnical Commission, May 1992.

[28] L. Malesani, P. Mattavelli, and S. Buso, "On the applications of active filters to generic loads," in *8th International Conference on Harmonics and Quality of Power. Proceedings (Cat. No.98EX227)*, vol. 1, pp. 310–319 vol.1, Oct. 1998.

[29] H. Akagi, E. H. Watanabe, and M. Aredes, *Instantaneous Power Theory and Applications to Power Conditioning*. Hoboken, NJ, USA: John Wiley & Sons, Inc., Feb. 2007.

[30] J. G. Ziegler and N. B. Nichols, "Optimum Settings for Automatic Controllers," *Journal of Dynamic Systems, Measurement, and Control*, vol. 115, no. 2B, p. 220, 1993.

[31] J. Richalet, A. Rault, J. L. Testud, and J. Papon, "Model predictive heuristic control: Applications to industrial processes," *Automatica*, vol. 14, pp. 413–428, Sept. 1978.

[32] S. Abrashov, T. B. Airimitoaie, P. Lanusse, F. Aioun, R. Malti, X. Moreau, and F. Guillemard, "Model Predictive Control Tuning: Methods and Issues. Application to steering wheel position control," *IFAC-PapersOnLine*, vol. 50, pp. 11331–11336, July 2017.

[33] S. Boyd and L. Vandenberghe, *Convex Optimization*. Cambridge: Cambridge University Press, 2004.

[34] J. M. Maciejowski, *Predictive Control: With Constraints*. Harlow [u.a.]: Prentice Hall, 2002.

[35] S. Boyd, N. Parikh, E. Chu, B. Peleato, and J. Eckstein, "Distributed Optimization and Statistical Learning via the Alternating Direction Method of Multipliers," *Found. Trends Mach. Learn.*, vol. 3, pp. 1–122, Jan. 2011.

[36] D. Dimitrov, A. Sherikov, and P. Wieber, "A sparse model predictive control formulation for walking motion generation," in *2011 IEEE/RSJ International Conference on Intelligent Robots and Systems*, pp. 2292–2299, Sept. 2011.

[37] J. L. Jerez, E. C. Kerrigan, and G. A. Constantinides, "A condensed and sparse QP formulation for predictive control," in *2011 50th IEEE Conference on Decision and Control and European Control Conference*, pp. 5217–5222, Dec. 2011.

[38] J. L. Jerez, E. C. Kerrigan, and G. A. Constantinides, "A sparse and condensed QP formulation for predictive control of LTI systems," *Automatica*, vol. 48, pp. 999–1002, May 2012.

[39] B. Fornberg, "Generation of finite difference formulas on arbitrarily spaced grids," *Mathematics of Computation*, vol. 51, no. 184, pp. 699–706, 1988.

[40] A. V. Oppenheim, *Discrete-Time Signal Processing*. Pearson Education, 1999.

[41] I. R. Khan and R. Ohba, "Closed-form expressions for the finite difference approximations of first and higher derivatives based on Taylor series," *Journal of Computational and Applied Mathematics*, vol. 107, pp. 179–193, Feb. 1999.

[42] C. Beltrán, J.-P. Dedieu, G. Malajovich, and M. Shub, "Convexity Properties of the Condition Number," *SIAM Journal on Matrix Analysis and Applications*, vol. 31, pp. 1491–1506, Jan. 2010.

[43] C. Cateriano Yáñez, G. Pangalos, and G. Lichtenberg, "Model predictive load compensation in distribution grids," 2017.

[44] A. Yazdani and R. Iravani, "A generalized state-space averaged model of the three-level NPC converter for systematic DC-voltage-balancer and current-controller design," *IEEE Transactions on Power Delivery*, vol. 20, pp. 1105–1114, Apr. 2005.

[45] B. Stellato, G. Banjac, P. Goulart, A. Bemporad, and S. Boyd, "OSQP: An Operator Splitting Solver for Quadratic Programs," *ArXiv e-prints*, Nov. 2017.

[46] A. A. Chihab, H. Ouadi, F. Giri, and T. Ahmed-Ali, "Adaptive non-linear control of three-phase four-wire Shunt active power filters for unbalanced and nonlinear loads.," *IFAC Proceedings Volumes*, vol. 47, no. 3, pp. 5061–5066, 2014.

Glossary

List of Acronyms

AC	alternating current
ADMM	alternating direction method of multipliers
APF	active power filter
DC	direct current
IRP	instantaneous reactive power
LSSS	linear state signal shaping
LQR	linear quadratic regulator
MPC	model predictive control
ODE	ordinary differential equation
PCC	point of common coupling
PLL	phase locked loop
PQ	power quality
PV	photovoltaic
PWM	pulse width modulation
QP	quadratic program

RHC receding horizon control

RMS root mean square

SAPF shunt active power filter

SNR signal to noise ratio

SRF synchronous reference frame

THD total harmonic distortion

VSC voltage source converter